

Evaluation of Frictional Characteristics of Precision Machined Surfaces

A Thesis
Presented to
The Academic Faculty

by

Richard C. Kalil, Jr.

In Partial Fulfillment
of the Requirements for the Degree
Master of Science in Mechanical Engineering

Woodruff School of Mechanical Engineering
Georgia Institute of Technology
May 2004

Atlanta, Georgia

Evaluation of Frictional Characteristics of Precision Machined Surfaces

by

Richard C. Kalil, Jr.

Approved by:

Dr. Shreyes N. Melkote

Dr. Thomas R. Kurfess

Dr. Steven Danyluk

May 24, 2004

Table of Contents

Acknowledgements	v
List of Tables	vi
List of Figures	vii
Summary	ix
Chapter 1 Introduction	1
1.1 Problem Statement	1
1.2 Benefits of Solution	3
1.3 Research Goal and Objectives	4
1.4 Thesis Outline	5
Chapter 2 Literature Review	7
2.1 Surface Characterization	7
2.1.1 Amplitude Parameters	10
2.1.2 Spatial Parameters	11
2.1.3 Hybrid Parameter	16
2.2 Effect of Texture on Lubrication and Friction	17
Chapter 3 Experimental Rig Design	20
3.1 Test Rig Design and Construction	21
3.2 Design Parameter Details	23
3.3 Load and Friction Data Processing	30
3.4 Summary	32

Chapter 4 Three-Dimensional Surface Characterization	33
4.1 Surface Measurement	33
4.2 Three-Dimensional Surface Parameter Results	36
4.3 Summary	50
Chapter 5 Results and Discussion	52
5.1 Experimental Design	52
5.2 Experimental Results	66
5.3 Evaluation of Results	70
5.4 Summary	75
Chapter 6 Conclusion	76
6.1 Summary of Findings	76
6.2 Future Work	79
Appendix A: Computational Code	81
Appendix B: DOE and Raw Data	86
References	88

Acknowledgements

I must first thank the Lord, Jesus Christ, for the sacrifice he offered to save me from my sinful nature. Without this most generous of gifts, all efforts in this world would be meaningless. I hope that I have followed in his will and conducted myself in a way that has pleased him and helped to advance his kingdom.

My most ardent and humble thanks goes to my parents, Mary and Richard, Sr. whose sacrifices for my siblings and I show the purest nature of selflessness and love. I cannot at present comprehend that which they have given up so that Jenni, Matt, and I could lead such charmed lives, but I hope that I can someday repay them with love and sacrifice of my own. They are truly children of Christ and his love for others shines in their actions every day. I hope that I have made you both proud in my work and in my deportment with those I meet along the way, and I ask that you would continue to guide me with your wisdom and love.

I also must thank those people at Georgia Tech without whom I would never have finished this work. Dr. Shreyes Melkote was my advisor and guide throughout the research process and his dedication to his work and to his students is evident to us all. Steven Sheffield helped me in every step of the design and construction of the testing apparatus and his expertise was invaluable to its completion. My office mates Sathyan, Kai, and especially Ramesh kept me sane with their companionship and were always willing to help when I was at a loss. Thank you all and may God bless you.

List of Tables

Table 2.1: Three-dimensional Parameters from Stout [6]	9
Table 3.1: Torque Calibration Chart	30
Table 4.1: Amplitude Parameters	37
Table 4.2: Spatial Parameters	47
Table 4.3: Hybrid Parameter	50
Table 5.1: Factors and Levels in Experiment	53
Table 5.2: Pressure-Viscosity Relationship	55
Table 5.3: Hertzian Contact Details	59
Table 5.4: Plasticity Indices	59
Table 5.5: Parameters Pre- and Post-testing	61
Table 5.6: Coefficient of Friction and 3-D Parameters	70

List of Figures

Figure 2.1: Texture Direction Defined	15
Figure 2.2: Typical Angular Spectrum Plots	16
Figure 3.1: Working Principle of Test Setup	21
Figure 3.2: Experimental Setup	23
Figure 3.3: Load Application Slide	25
Figure 3.4: Roundness Error Load Variation	27
Figure 3.5: Load Cell Calibration Plot	28
Figure 3.6: Poor Axial Alignment	29
Figure 3.7: Shaft Support Bearings	30
Figure 4.1: Grayscale Images	35
Figure 4.2: Topographic Maps	35
Figure 4.3: AACF Plots	40
Figure 4.4: APSD Plots	44
Figure 4.5: Texture Direction Defined	45
Figure 4.6: Angular Spectra	46
Figure 5.1: Flow Curve for SAE 5W-30	55
Figure 5.2: Grayscale and Topography of HT Surface	61
Figure 5.3: PSD Plot for Typical Load Signal	64
Figure 5.4: Filtration of Load and Torque Data	65
Figure 5.5: Coefficient of Friction Results	67

Figure 5.6: Mean Coefficient of Friction by Surface	68
Figure 5.7: Predicted and Actual Friction Coefficients	70

Evaluation of Frictional Characteristics of Precision Machined Surfaces

Richard C. Kalil, Jr.

Advised by Dr. Shreyes N. Melkote

Precision surface finishes are used in a wide variety of applications. From bearing races and rolling elements to parallel slide ways, the frictional characteristics of these surfaces are critical to the performance of the products. Experimental trial and error has shown that certain surfaces outperform others in certain applications, but the specific surface characteristics that make this true have yet to be fully understood. The research goal was to develop an apparatus that can test the coefficient of rolling/sliding friction of different precision machined surfaces and to combine this data with topographic analysis of the surfaces to correlate specific 3-D parameters with the frictional performance of a surface.

The sample treatments consisted of four different surface textures (hard-turned, ground, honed and isotropic finish) and four different relative surface speeds. By monitoring the torque in the sample-mounting shaft under lubricated conditions the coefficient of rolling/sliding friction of each surface was found. Utilizing white light interferometry measurement of the surfaces, a highly detailed map of each surface was obtained.

Using different characteristic values of each machined surface (RMS roughness, asperity density, lay direction, etc.), the frictional behavior of the surfaces were compared to the surface characteristics yielding insight into the relationship between surface finish and friction in rolling/sliding contact. Friction coefficient was found to correlate most strongly with RMS roughness (S_q) and density of surface summits (S_{ds}). These parameters govern mechanical interference of asperities and surface adhesion respectively. These findings suggest that friction coefficients of surfaces could be optimized through manipulation of three-dimensional surface parameters.

Chapter 1

Introduction

1.1 Problem Statement

In the design and manufacture of any component, many factors must be closely monitored. Obviously, the functional portions of all parts must fit into strict size tolerance specifications in order to operate in the desired roles; grooves must fit snugly around tongues while proper clearance is maintained for moving pieces. Also, the designer of a part will usually specify a desired surface finish. While it is widely known that some machined surfaces (ground, turned, etc.) outperform others in certain roles, this knowledge is largely qualitative. For instance, in the bearing industries the roughness characteristics of a surface are often used to suggest its behavior. Parameters such as wear, friction, and lubricant retention are often attributed to a surface's roughness. While roughness does play a significant role in each of these areas, this thinking disregards many of the texture facets that may be equally as important. Texture is defined as periodic or random deviations of the actual surface from the nominal surface. It consists of roughness, waviness, lay, and surface flaws [1].

Among the most important features of precision finished surfaces in general and specifically roller element bearings is their coefficient of

friction. While experience may show that a surface with smaller roughness yields a lower coefficient of friction than one with larger roughness, comparatively little is known that will predict the behavior of two surfaces of similar roughness that have differing texture characteristics. These texture parameters are three-dimensional in nature and are vital in continuing to understand the volumetric nature of contact in moving parts.

In the past, researchers have used two-dimensional surface characterization to analyze frictional response in point contact. Usually this involves dragging a diamond stylus over the surface to generate a 2-dimensional picture of the texture and subsequently drawing a normally loaded probe across the same line while measuring the resisting frictional force. This approach does not, however, take into account line or larger surface area contacts, leaving many questions unanswered for the majority of designers. For example, in the design and production of roller bearings, friction coefficients are extremely important to the operation of the parts. In the rolling/sliding friction event taking place between the rolling element and race, surface finish plays a vital role in determining the bearing's frictional response. Unfortunately, the effect of three-dimensional texture of the mating surfaces on the coefficient of rolling/sliding friction is not fully understood. Again, over years of bearing production some surface finishing processes have shown themselves

advantageous over others, but the parameters of the finish itself that would maximize performance are largely unknown. The problem addressed here then lies in the correlation of three-dimensional surface parameters with the fluctuations in a surface's coefficient of rolling/sliding friction.

1.2 Benefits of Solution

With this correlation in hand, a designer would wield unparalleled control over the behavior of his parts. Using different precision machining processes an improved coefficient of friction could be achieved to maximize the performance of each surface. In the example of ball and roller bearing production, even tiny gains against friction losses will result in the following:

- Less heat production leading to lower cooling costs
- Smoother operation leading to more efficient power use and lower loads
- Less wear leading to longer bearing life

These improvements would certainly have a dramatic impact on the bearing production industry as well as that of any manufacturer who battles friction losses in design and production.

In addition to improving surface performance by combining different known finishing processes, an entirely new finishing process could

be reverse engineered to optimize the surface parameters that most affect performance. If a particular texture is shown to be ideal for cylindrical roller bearings for example, and current processes will not produce said finish, a process could be designed to finish the races and rolling elements that minimizes asperity contact and plastic deformation while maximizing lubrication without decreasing load-carrying capacity. This would lead to components that improve the operation of the assembly without any significant changes to their overall design. A concept that engineers, as well as stockholders, are sure to appreciate.

1.3 Research Goal and Objectives

The purpose of this research is to identify significant 3-D surface texture parameters that directly affect the coefficient of rolling/sliding friction. Through the correlation of the surface characteristics of common precision finishing processes with their respective coefficients of friction, the most important facets of these finishes with respect to friction will be revealed.

The first step in accomplishing this goal was to design an apparatus that could measure the coefficient of rolling/sliding friction on different surfaces. The theory of operation and design strategy of this rig will be discussed in detail later in Chapter 3.

Next, a method to measure the 3-D parameters of each surface tested was chosen. The requirements of this strategy are to collect three-dimensional surface texture data that are easily transferred to a software analysis package that will isolate the different parameters. The data collection system must have nanometer level resolution to capture the true microscopic nature of the surfaces and the ability to translate this data into a topographic map useful for analysis. The details of this strategy and its implementation will be discussed in Chapter 4.

The data collected from both the friction testing rig and the surface characterization equipment are then analyzed to accomplish the overall goal of the research stated above.

1.4 Thesis Outline

This thesis will be organized in the following fashion. Chapter two will consist of a literature review of pertinent work in the areas of surface characterization and friction related research. It identifies work that relates to the topic of surface parameters and their effect on friction and highlight areas that this thesis will expand. Chapter three will describe the working principle and design of the experimental test rig and also the data acquisition strategy of that system. Chapter four will present the method of collection of surface map data and the 3-D surface parameters computed for each finish in question. Chapter five contains

the experimental design, correlated results, and possible explanations of the findings. Finally, chapter six will summarize those findings, outline new questions raised by this research, and suggest future work that will likely be needed to further enhance the understanding of surface texture's effect on friction.

Chapter 2

Literature Review

It is commonly known that the roughness or smoothness of a surface will affect its frictional behavior. While generally characterizing a surface as 'rough' or 'smooth' will lend some idea as to how it will perform in a frictional capacity, a lack of understanding the phenomena involved in the surface's interaction with another prevents optimization of the system. In order to better understand the interaction between contacting surfaces, it is essential to know the true nature of the surface. Research dedicated to more exact and descriptive surface characterization has been underway for many years in order to more perfectly model the true nature of surfaces. Many two-dimensional parameters have been defined in US and international standards [2,3]. A review of this body of research begins this chapter followed by past work concerning frictional characteristics of surfaces and lubrication. From this review, the pertinence of this thesis will become evident and the purpose of the research made clear.

2.1 Surface Characterization

Research in the area of surface characterization is by no means a new and original topic. In its earliest stages, surface characterization work

was limited to two-dimensional parameters. In most cases a diamond stylus was drawn across a surface and an LVDT or similar sensor would detect the small peaks and valleys along a certain line on the surface. The data collected from the sensor would then be used to make a surface profile or cross-section along the line of measurement.

While stylus size concerns often cast a shadow of doubt upon valley measurement accuracy [4], this form of data collection proved generally effective in evaluating the nature of a surface. With a clearer qualitative picture of the actual surface, researchers sought a method for characterizing each surface so that it might be compared to others quantitatively. In his book, Rough Surfaces, Thomas [4] presents and explores an extensive list of quantitative values that can be computed from a two-dimensional surface plot. Certainly these parameters were and are very helpful in gaining insight into the true nature of a surface, but they leave much to be desired in true characterization because surfaces are inherently three-dimensional. If the 2-D surface profile is made on a particularly smooth or rough portion, it will skew the perceived roughness of that surface. Also, a simple line-based profile cannot yield information about lay patterns or consistency across the remainder of the surface. Certainly, to study a surface accurately, one must characterize an area having both length and width.

This leads to the next stage in surface characterization: three-dimensional parameters. Upon the realization that surfaces interact in three-dimensions instead of two [5], a set of fourteen parameters was proposed by Stout et al. [6]. Four describe the amplitude of the surface imperfections, four describe spatial properties, three describe a combination of the two, and three describe functional characteristics. Table 2.1 shows the set of three-dimensional parameters set forth by Stout et al. organized by type.

Table 2.1 - Set of 14 3-D parameters given by Stout et al. [6]

Amplitude Parameters	Spatial Parameters	Hybrid Parameters	Functional Parameters
RMS Deviation S_q	Density of Summits S_{ds}	RMS Slope $S_{\Delta q}$	Surface Bearing Index S_{bi}
Ten point Height S_z	Texture Aspect Ratio, S_{tr}	Mean Summit Curvature S_{sc}	Core Fluid Retention Index S_{ci}
Skewness S_{sk}	Texture Direction S_{td}	Developed Area Ratio S_{dr}	Valley Fluid Retention Index S_{vi}
Kurtosis S_{ku}	Fastest Decay Autocorrelation Length S_{al}		

These parameters are discussed in great detail by Stout et al. [6, 7, 8, 9] and Dong et al. [5, 7, 8]. In their work, they identify the parameters that tend to be most important to the functionality of a surface. In the

following sections, their research of the three-dimensional parameters most important to this work will be discussed.

2.1.1 Amplitude Parameters

Root Mean Square Deviation of Surface Topography (S_q)

This statistical amplitude parameter is analogous to the 2-D average roughness parameter, R_a . It is defined as the root mean square (RMS) value of the surface asperity departures from the reference nominal surface height. This parameter gives a conservative estimate of the average asperity height of the surface being measured. This parameter is most fundamental in the characterization of a surface in that it directly relates to the degree of smoothness relative to a perfectly flat nominal surface height.

Skewness of Topography Height Distribution (S_{sk})

This parameter measures the asymmetry of surface deviations about the mean reference plane. Most material removal processes will tend to have negative skewness values because their surfaces are dominated by troughs and valleys whereas additive processes are more likely to be peak and spike dominant resulting in highly positive skewness. Skewness is often unstable for indicating the functional properties of a

surface because its value can be greatly affected by a small number of abnormally tall peaks or abnormally deep valleys.

2.1.2 Spatial Parameters

Owing to the fact that two-dimensional parameters cannot capture the degree of isotropy of a surface area, three-dimensional spatial parameters must be applied. Both deterministic and random surfaces can have decided isotropic or anisotropic character, so these parameters can help more accurately compare surfaces. Difficulty arises in computing these parameters because many surfaces have high order frequency components with often multi-wavelength composition. These three-dimensional texture parameters involve detailed areal autocorrelation function (AACF) and areal power spectral density (APSD) analyses to identify lay patterns and texture characteristics.

AACF and APSD Analyses

The autocorrelation function (ACF) depends on the notion that surface profile readings can be treated as random signals. Peklenik [10, 11] first proposed computing various random process functions for machined surfaces. An exponentially decaying ACF was proposed by Whitehouse and Archard [12] to model a random Gaussian surface. Nayak [13, 14] analyzed Gaussian surfaces by using AACF and APSD to

define its spectral moments. Sherrington [15, 16] used APSD to analyze surface patterns and Dong et al. [7] employed AACF and APSD to characterize spatial parameters in three dimensions on engineering surfaces.

Spectral analysis condenses data in the space domain into a frequency-based domain. By exploring the possible periodic nature of data, particular individual frequencies or wavelengths can be isolated as having primary contribution to the shape of the surface. High spatial frequency components will contribute more to the roughness and low spatial frequencies to the waviness of the surface. The presence and density of these classes of frequencies provide insight into the surface's dominant features. Sherrington [15, 16] first explored two-dimensional spectrum analysis of an engineering surface. Also, Lin et al. [9] proposed methods for determination of the frequency bandwidth for three-dimensional spectral analysis while Dong et al. [8] discussed the Hermitian symmetry for two-dimensional spectral analysis and an algorithm to compute the APSD and extract texture parameters.

Fastest Decay Autocorrelation Length (S_{dl})

This parameter seeks to identify the shortest distance from the origin that the normalized AACF decays to a value of 0.2. Whitehouse and

Archard [12] used a fastest autocorrelation value of 0.1 for an exponentially decaying random Gaussian surface. Since actual surfaces seldom display exponential decay, Dong et al. [7] used the proposed decay value of 0.2 for the normalized AACF. This parameter identifies the direction in which correlation is minimized and therefore identifies the direction perpendicular to the lay pattern, as correlation is largest along the lay. Also, the rate of decay yields insight into the dominant frequencies of the surface. Surfaces that are highly wavy (low frequency dominant) have long correlation lengths whereas rougher, flatter (high frequency dominant) surfaces have very short S_{al} .

Density of Summits (S_{ds})

This parameter represents the number of summits contained in the sampling area. Summit definition carries vital importance in the usefulness of this parameter. Here, a summit is the highest point in an area that lies consistently above the mean height of the sampling region. Ambiguity abounds in the definition of sampling region, however. Many definitions exist such as 'nearest eight neighbors' [4]. Thomas [4] showed that S_{ds} increases with sampling frequency. When using a high-resolution characterization process, such as white light interferometry, the micro-area peaks could be considered summits although they will not likely affect contact. For example, in the troughs of a hard-turned surface the

local peaks are well below the contacting surface of the sample, but a high-resolution surface map will likely point them out as summits. This problem requires a more stringent definition of a summit. Dong et al. [7] suggests using S_{dl} and S_{ds} to define a sampling area. This method greatly reduces sampling resolution's effect on summit definition. The sampling area is set as a square whose sides' half-lengths are equal to S_{dl} . This method takes into account the lay pattern of the surface and avoids identification of local peaks as summits by sizing the sampling area to include longer wavelength roughness components.

Texture Aspect Ratio (S_{tr})

This parameter identifies the level of isotropy of a surface. If a surface is decidedly anisotropic, S_{tr} can reveal the presence of texture pattern or long-crestedness. A value of S_{tr} greater than 0.5 indicates strong isotropic nature while a value smaller than 0.3 indicates anisotropy in the surface. For example, a random surface shows no discernable pattern in any direction across its lay and will therefore have a high S_{tr} value (isotropic), but a highly ordered surface (i.e. a turned surface) has a definite pattern of parallel troughs and peaks in one direction across the surface and will have a low S_{tr} value (anisotropic).

Texture Direction (S_{td})

In the presence of a lay pattern, this parameter indicates its pronounced direction. This information is extracted from the APSD. Since the coordinate system of the surface is arbitrary [7] it is defined as shown in Figure 2.1.

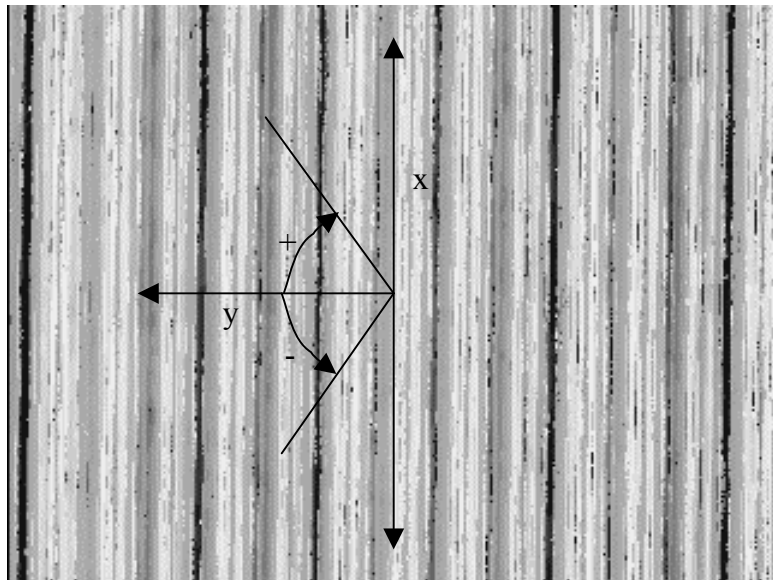


Figure 2.1: Texture Direction Defined

The texture direction is given by the angle of maximum power in the angular spectrum plot. For a lay pattern perpendicular to the Y-axis, the maximum power will lie at 90° (Figure 2.2(a)) whereas an isotropic surface will show no definitive angle of texture direction (Figure 2.2(b)).

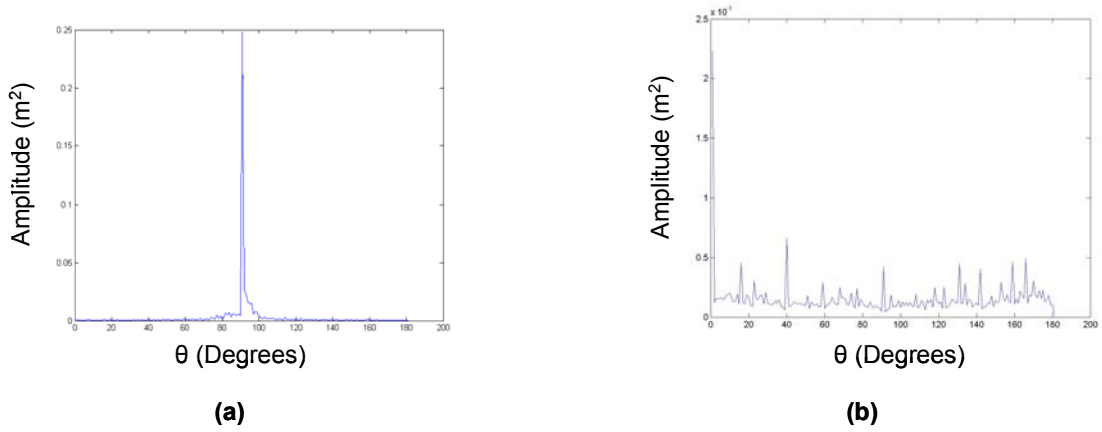


Figure 2.2 Typical Angular Spectrum Plots for Highly Anisotropic (a) and Highly Isotropic (b)

2.1.3 Hybrid Parameter

RMS Slope ($S_{\Delta q}$)

The root mean square slope of a surface identifies the steepness of the sides of asperities. For example, if a representative asperity has a shape like that of a sand dune, with gradual height changes in all directions away from the peak, its slope will be rather small. Alternately, if a representative asperity's shape resembles a tall cone with a small base radius, having drastic height changes in all directions away from the peak, its slope will be rather large. The possible range of slopes lies between zero (for a perfectly flat surface) and one (for a surface with vertical walls defining asperities). The surface parameters in this section will be computed for each surface. These data will appear later in

Chapter 4 when the specific topographic differences between the surfaces are discussed.

2.2 Effect of Texture on Lubrication and Friction

The friction and lubrication work that has been done in the past is much more intuitive in nature than the three-dimensional characterization work. Due to its lack of complicated surface parameter definitions, this portion will be much more brief than the previous section. The work contained here tends to be much more experimental in nature and therefore relates very directly to the scope of this work.

The texture of a surface can affect the lubrication conditions of that surface. Patir and Cheng [17] in 1978 found that texture direction affects lubricant flow and the build up of lubricant films. Esfahanian and Hamrock [18] classified elastohydrodynamic lubrication (EHL) regimes based on the levels of elastic deformation in the asperities of a surface. Zhu [19] further postulated that roughness does not significantly change the fluid film thickness in surfaces under the same speed, load, and gap conditions. Hamrock and Cheng [20] studied the existence and effect of surface predictors for the breakdown of EHL in non-conformal surfaces like roller element bearings. Also, Zhu, Cheng, and Hamrock [21] explored pressure spikes in EHL contact and their location and intensity for different roughness and texture orientations.

A model for rough surface contact was developed by Greenwood and Williamson in 1966 [22]. Their main concern was with the changes in contact area with increased loads. The effect of surface topography on friction has been studied extensively both experimentally and with analytical/simulation tools. Hisakado [23] studied the friction characteristics of rough surfaces in contact under boundary lubrication conditions while Johnson et al. [24] explored friction between rough surfaces under EHL conditions. Rabinowicz [25] correlated friction with RMS roughness and sliding speed for dry sliding contacts. Experimental study conducted by Jeng [26] confirmed the dependence of friction on lay direction, speed and load under lubricated conditions. He postulated that asperities oriented perpendicular to the direction of surface motion would resist lubricant flow and help build up a larger supporting film. He referred to this process as “flow visualization technique.” These tests were made under ball-on-disc contact conditions in pure sliding. Koura [27] found that surface friction increased with average roughness and Cann et al. [28] correlated behavior in the Hertzian contact zone with roughness and asperity density. Holmberg [29] investigated the effect of surface topography on friction under low speed rolling/sliding contact. These tests yielded similar results to Jeng’s work, except that a rolling/sliding disc-on-disc apparatus was used. This apparatus is comparable to the system used for the experiments in this work. He explains his results by a

“hydrostatic lubrication effect” and a “squeeze film lubrication effect.” Cheng [30] and Tripp et al. [31] studied the effect of transverse and longitudinal roughness on EHL. They explored the changes in lubricant film thickness as the texture direction was oriented differently with respect to the surface motion. The effect of texture and roughness was further explored by Ai et al. [32], Zhu et al. [33,34], and Lubrecht et al. [35] under EHL point contact simulations. Most of these simulations focused on pressure profile and film thickness, but also include additional information such as sub-surface stress. While the majority of the past experimental work is based on 2-D surface characterization, Singh and Melkote [36] studied the correlation of three-dimensional surface parameters of precision finished surfaces with coefficient of pure sliding friction in a ball-on-disc setup. They found that root mean square roughness, density of surface summits, and texture direction most directly affect the coefficient of friction. This work will build directly upon theirs by attempting to correlate three-dimensional surface parameters of precision finished surfaces with their coefficients of rolling/sliding friction in line contact. The use of these 3-D parameters for precision finished, real surfaces and the evaluation of their effect on coefficient of rolling/sliding friction give this thesis a subject that is unique from the work done in the areas of surface characterization and friction response.

Chapter 3

Experimental Rig Design

In order to measure the coefficient of friction under rolling/sliding contact, an experimental apparatus was designed and constructed specifically for the task. The test rig operates by first placing two precision finished discs in contact with each other on their outer circumferential surfaces under a normal load and then rotating the discs about their axes at different speeds producing a relative surface speed between them. A simple schematic of this idea can be seen in Figure 3.1. The resulting torque measured in the shaft supporting one of the discs is combined with the radius of that disc to yield the force of friction between the surfaces. Finally, the normal load divides the torque to yield the measured coefficient of friction. The details of this system follow.

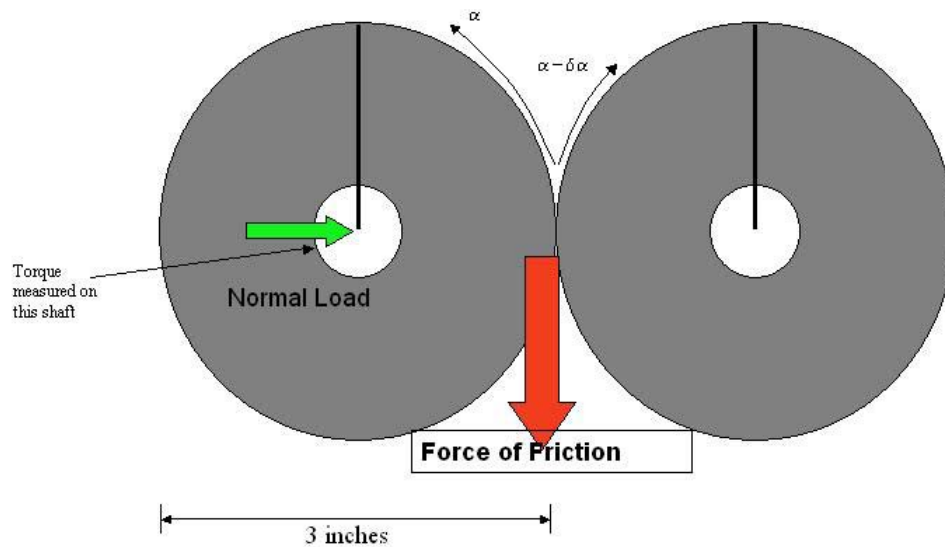


Figure 3.1: Working Principle of Test Setup

3.1 Test Rig Design and Construction

Figure 3.2 shows a photograph of the completed setup. The components that can easily be seen are two 220V/3P 2HP electric motors (Reliance Electric Model #P14A5805P) with their speed control units at the far left and right. These motors supply the driving force for the disc rotation and are electronically controlled to maintain constant speed. Following the drive shaft of the left motor, a semi-rigid Lovejoy coupling is evident in orange followed by a pair of alignment bearings rigidly mounted to two steel supports, which are bolted securely to the aluminum base plate. Between these bearings is where a test sample resides after

press fitting onto the mounting shaft. Following the drive shaft of the right motor, a strain-gage type torque transducer with 500 Hz frequency response (Omegadyne Model #TQ503R-10) is evident with red coloration, followed by a support bearing (green) and then a pair of alignment bearings with a test sample mounted between. These alignment bearings are rigidly bolted to an aluminum plate that is mounted on a precision slide-way (Thomson Model #2DA0800AL 10") below. At the bottom of the picture, four brass fittings feed compressed air to four pneumatic loading pistons (Dadco Model #C.090.025). These pistons are mounted on an aluminum plate supported by gussets. They apply pressure to another aluminum plate that contains a strain-gage based load cell with frequency response of 500 Hz (Omegadyne Model #LC305-200) sandwiched between the pistons and the test sample. Four steel rods that assure application of all loads from the pistons directly to the test sample mounting plate suspend the load cell housing plate. The load applied here is the source of the normal load on the line of contact between the test samples.

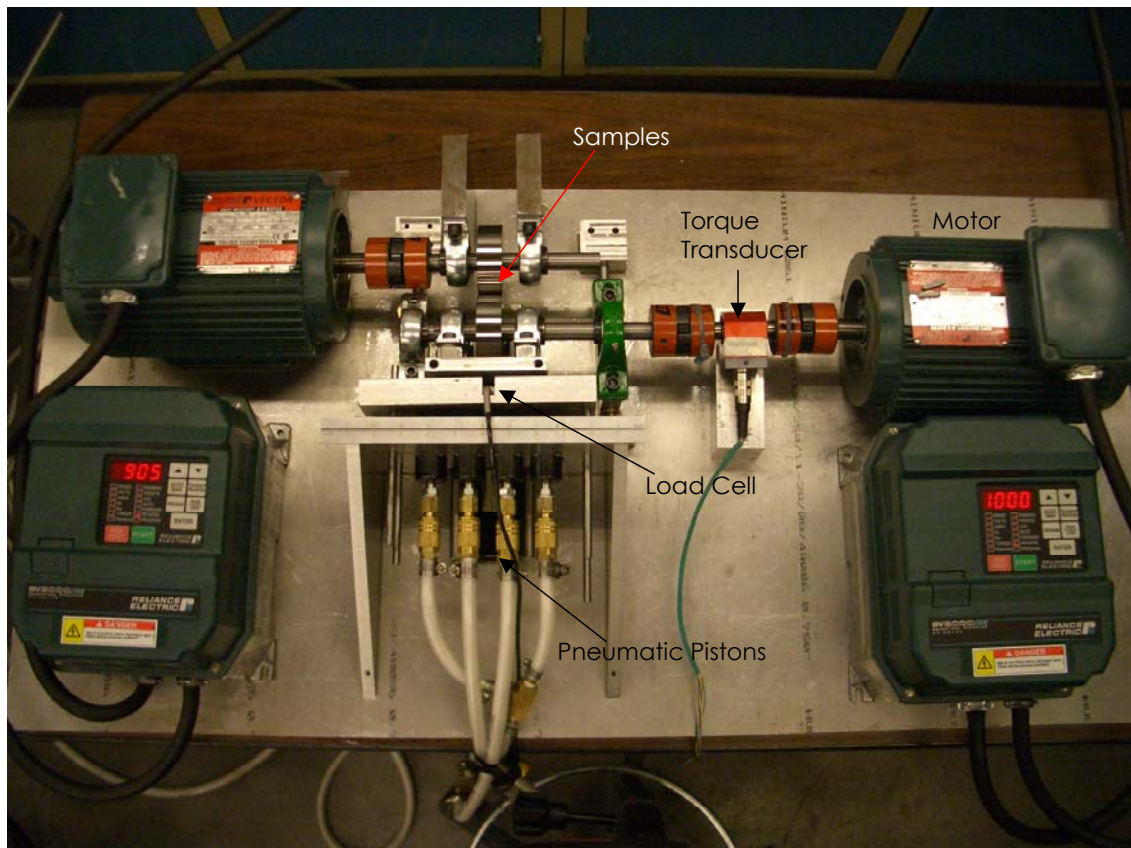


Figure 3.2: Experimental Setup

Now that the reader is oriented to the layout of the test rig, the specific design and function of each facet will be discussed.

3.2 Design Parameter Details

In the design of the rolling/sliding friction testing rig, two major functions were required: application and measurement of a radial load normal to the rotational axes and relative motion between the surfaces with measurement of their resistance to this motion. A mock bearing design was chosen for its industrial applicability as well as its ease of conducting prolonged tests without direction change. The major

drawback of this choice is certainly the prevalence of alignment and runout errors. These errors will be discussed in greater detail later. Referring back to Figure 3.1, notice the opposite directions of rotation (CCW on left, CW on right) and the differing surface speeds. This results in a true rolling/sliding condition common to bearing surfaces. Also note the normal load applied to the bearing on the left through its support shaft. This load should remain constant during any one test. Finally, the torque produced by the rolling/sliding contact is measured in the shaft of the left sample. These data combined with data collected from the load cell yield the coefficient of friction as a function of time during each test using the following equations:

$$F_f = \frac{T}{r} \quad (1)$$

$$\mu = \frac{F_f}{n} \quad (2)$$

where T is the measured torque, r is the radius of the sample, F_f is the force of friction, n is the normal load, and μ is the coefficient of rolling sliding friction.

The loading system for this apparatus was designed with a few very important parameters in mind. First and most importantly, the force measured by the load cell must accurately represent the load at the point of surface contact. This means that any components between the load cell and test surfaces must transmit forces without significant

absorption. Thus, the number of components between the load cell and sample was kept to a minimum by using only a solid aluminum plate supporting two steel alignment bearings. This plate moves freely in the radial direction of the samples by way of a precision ball bearing slide. This slide allows the plate and samples to move into the testing position using negligible force and without dampening the force applied to the system (Figure 3.3).

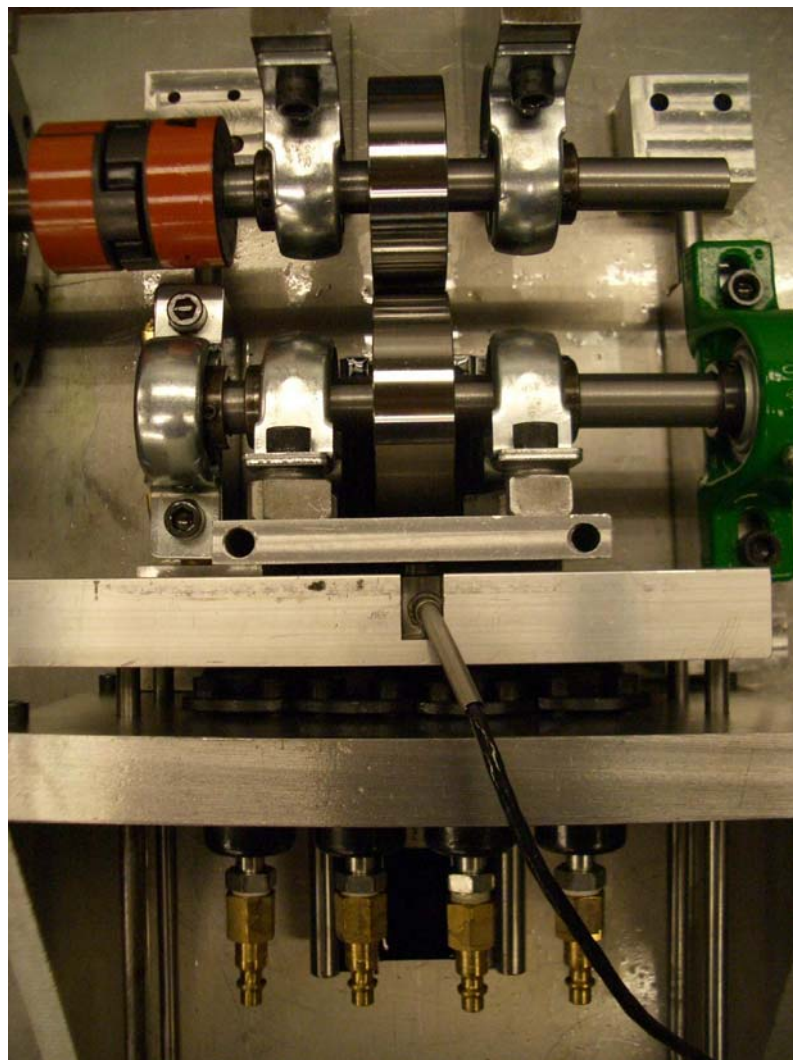
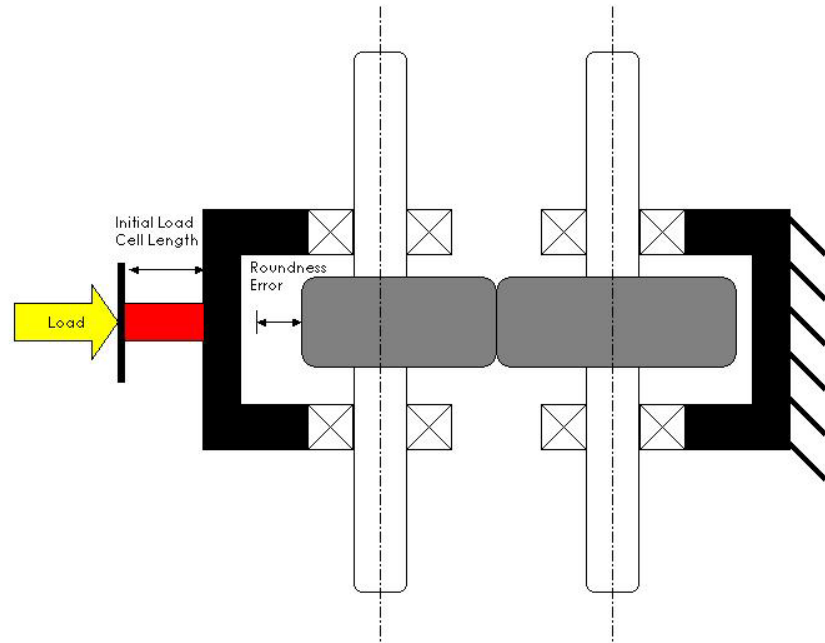
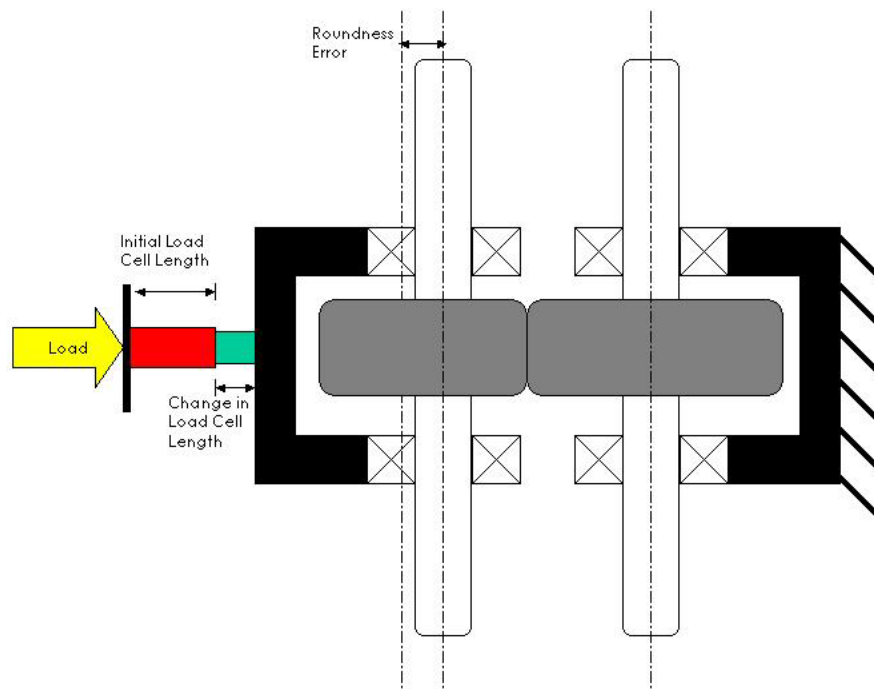


Figure 3.3: Load Application Slide

Second, a constant applied force is desired. A pneumatic piston system with variable pressure control was chosen to fulfill this requirement. The bottom of Figure 3.2 shows the group of four pistons in perpendicular alignment to the load cell housing plate. Also, because the load cell is essentially a strain-gage transducer, tiny changes in its length register as changes in loads. Therefore, the samples must have very little runout error ($<25\mu\text{m}$ total runout) as well as near-perfect alignment. Otherwise, when a low point (reduced radius) on one sample comes into contact with the other sample, the movable sample will pull away from the load cell, increasing its length and effectively decreasing the measured load (and the opposite when a high point is reached). An illustration of this idea can be seen in Figure 3.4. The calibration plot for the load cell can be seen in Figure 3.5. The load cell was calibrated by loading up to its maximum rating and then unloading from that maximum back to zero load. Finally, the desired load range is one to one hundred pounds and a standard air compressor (~ 140 psi max) easily supplies this through the pneumatic pistons.



(a)



(b)

Figure 3.4: Roundness Error Load Variation
(a) Initial condition and (b) after 180° shaft rotation

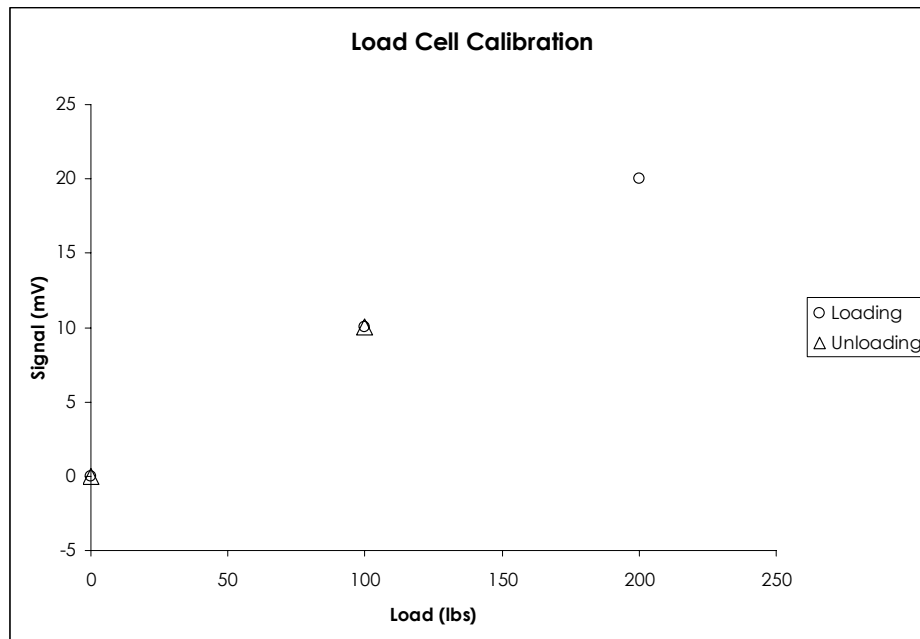


Figure 3.5: Load Cell Calibration Plot

The design of the sample drive system of this apparatus demanded attention to a few key parameters. First, the rotation of the two samples relative to each other must be made at constant surface speeds. A system without constant speed control would be nearly useless in determining the amount of sliding between the test samples under rolling/sliding conditions. Thus, high torque, constant speed motors were selected as the drive power source. These motors continually monitor their speed and apply or remove power to keep that speed constant within one RPM. Second, very careful alignment of the sample support bearings is crucial to the true line contact between the testing surfaces. If the axes of the sample discs are not parallel, only the edge of one sample would be in contact with the opposite surface, greatly reducing the area

of contact and nullifying the friction information obtained for line contact.

Figure 3.6 shows an illustration of poor axial alignment.

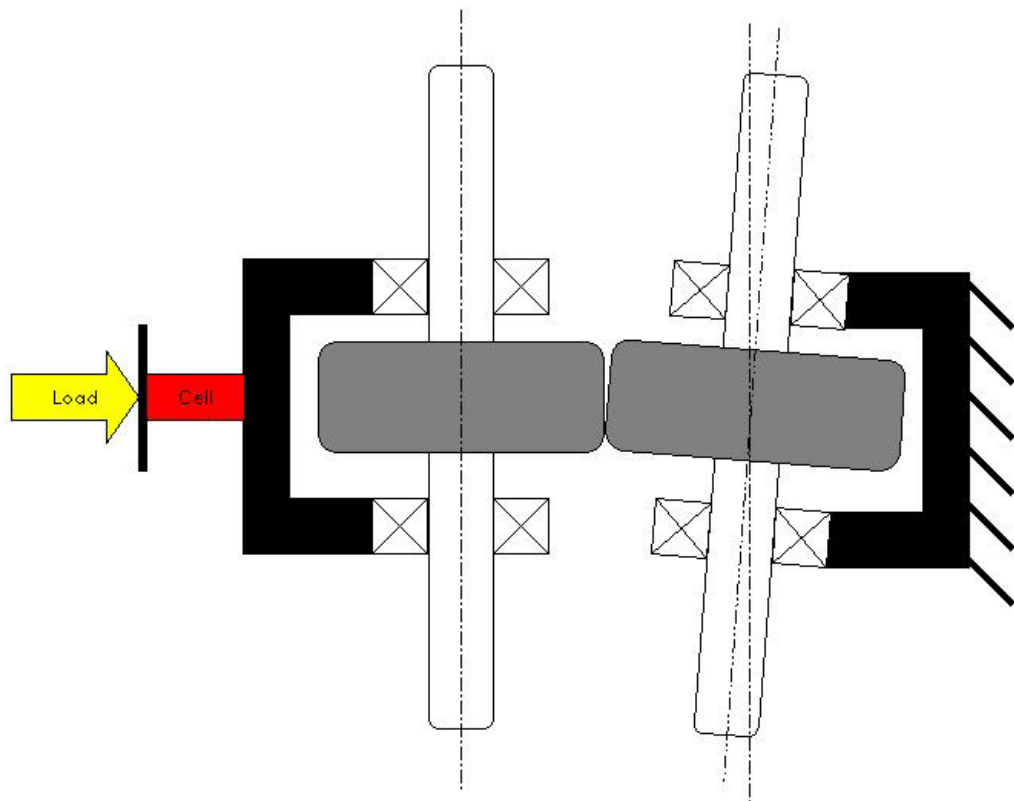


Figure 3.6: Poor Axial Alignment

Finally, vertical alignment of the samples with the line of load application is crucial. If the samples' centers are not in line with the normal force applied to them, one sample will tend to 'climb' the face of the other effectively lifting or lowering the movable sample's support plate. This will cause a cyclic loading and unloading of the samples that will result in inconsistent torque readings. To avoid this problem, rigidly mounted shaft support bearings were installed to run along stainless steel rails (Figure 3.7),

eliminating any vertical movement and ensuring consistent sample contact. Also, the torque transducer calibration data supplied by the manufacturer can be seen in Table 3.1.

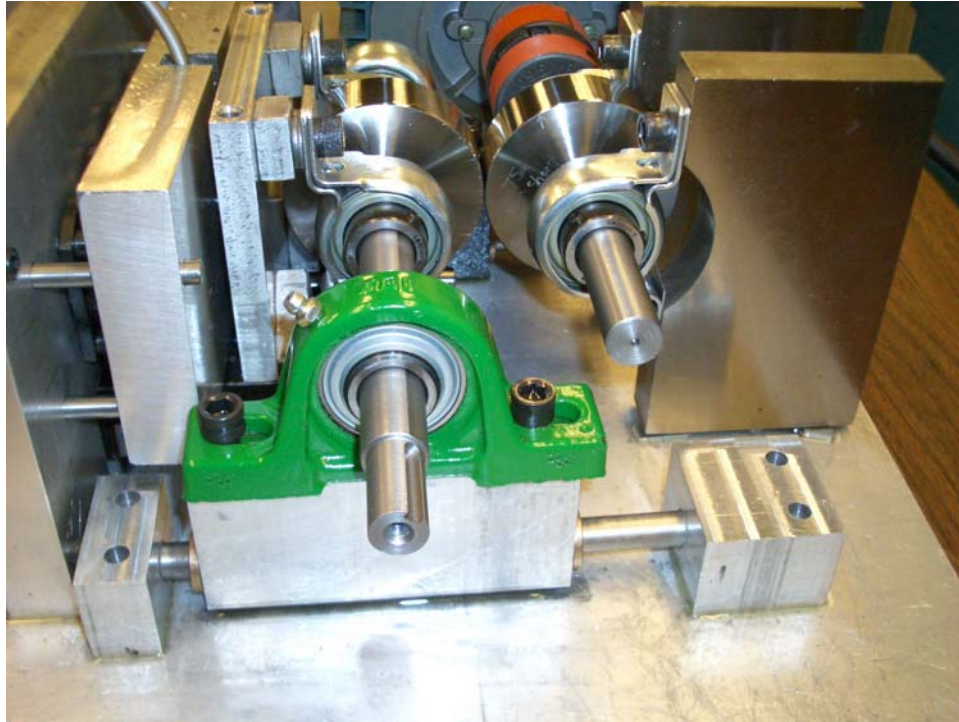


Figure 3.7: Shaft Support Bearings

Table 3.1: Torque Transducer Calibration Chart

Torque (Nm)	Signal (mV)
0	0.0000
10	2.0024

3.3 Load and Friction Data Processing

With data prepared to flow from the mechanical setup described above, a system for collecting and storing them was developed. This system consists of a National Instruments (NI) data acquisition (DAQ) card, a NI signal conditioning box, and a NI LabVIEW software code for converting voltage signals to torque and load data. The DAQ card

chosen is a model PCMCIA-6024E that features sixteen channels of analog input, two channels of analog output, a 68-pin connector and eight lines of digital input/output. Its maximum timing resolution is 50ns which is more than adequate for this application. The signal-conditioning box is a model SCB-68. Finally, a LabVIEW program for data processing was written to convert the voltage signals from the DAQ card into usable data in the form of Nm (torque) and N (load) using the calibration information supplied with the sensors.

Although great care was taken to avoid roundness error in the manufacture of the sample discs, no process could possibly yield perfectly round samples with perfectly concentric inner and outer diameter. As mentioned earlier and illustrated in Figure 3.4, these small run-out errors lead to a cyclical nature in the load and subsequently the torque measurements. The frequency of this cyclic measurement phenomenon matches the rotational speed of the monitored disc and a low-pass filter was applied just below the rotational speed to eliminate these predictable variations. The details of this procedure will be discussed later when the results are presented.

3.4 Summary

This chapter highlighted the design parameters and concerns of the experimental apparatus and the components that make up the data acquisition system. It showed the working principle behind the testing of rolling/sliding friction and precautions taken to ensure accurate simulation of such a situation.

Chapter 4

Three-Dimensional Surface Characterization

In order to correlate specific 3-D surface parameters with friction coefficient response, a system was needed to first accurately document the microscopic shape of each surface and second compute the different surface parameters of the test samples. A white light interferometry system was chosen for its accuracy and speed of measurement for the mapping of the surface shapes and a computer code (detailed in Appendix A) was written to translate the surface maps into three-dimensional surface parameter data. The details of the data collection and surface parameter comparisons are contained in this chapter.

4.1 Surface Measurement

White light interferometry employs interference patterns of polychromatic light to measure lengths on the order of nanometers. In the case of this research, the heights of discrete points filling an area .7mm by .53mm were measured to get an accurate topographic map of each surface under investigation. A 250 x 200 data matrix of surface height (z) in the x and y directions respectively was laid out within this mapped area. A second-order least square surface was then fit to the

data matrix to eliminate the form [37] and establish a reference datum. This effectively eliminates the macroscopic curvature of the cylindrical samples. This resulting surface height data matrix contains the information that was used to acquire the surface parameters mentioned in Chapter 2. After thorough preparation with a clean drying solvent, each sample was measured three times, once at a specific marked point and twice at random points, before its use in an experiment and again in the same manner after completion of the experiment. It is important to note here that no significant changes were observed in the surfaces after their use in an experiment. This fact will be discussed in greater detail in the following chapter. These values were then averaged and standard deviations recorded across every sample sharing a common finish to specify a single number for each parameter for each surface.

Figure 4.1 displays the gray scale images of each of the four precision-machined surfaces analyzed: Isotropic (IF) [38], Honed (HN), Hard-Turned (HT), and Ground (GD). Figure 4.2 contains the topographic maps for each of the surfaces. Note the differing height scale for each.

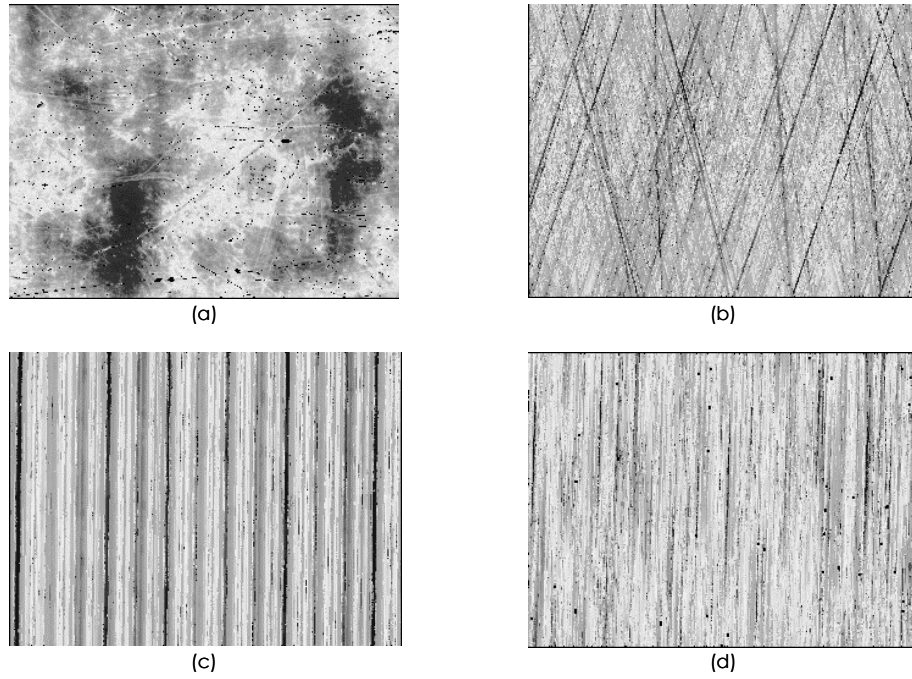


Figure 4.1: Gray Scale Images of (a) IF, (b) HN, (c) HT and (d) GD

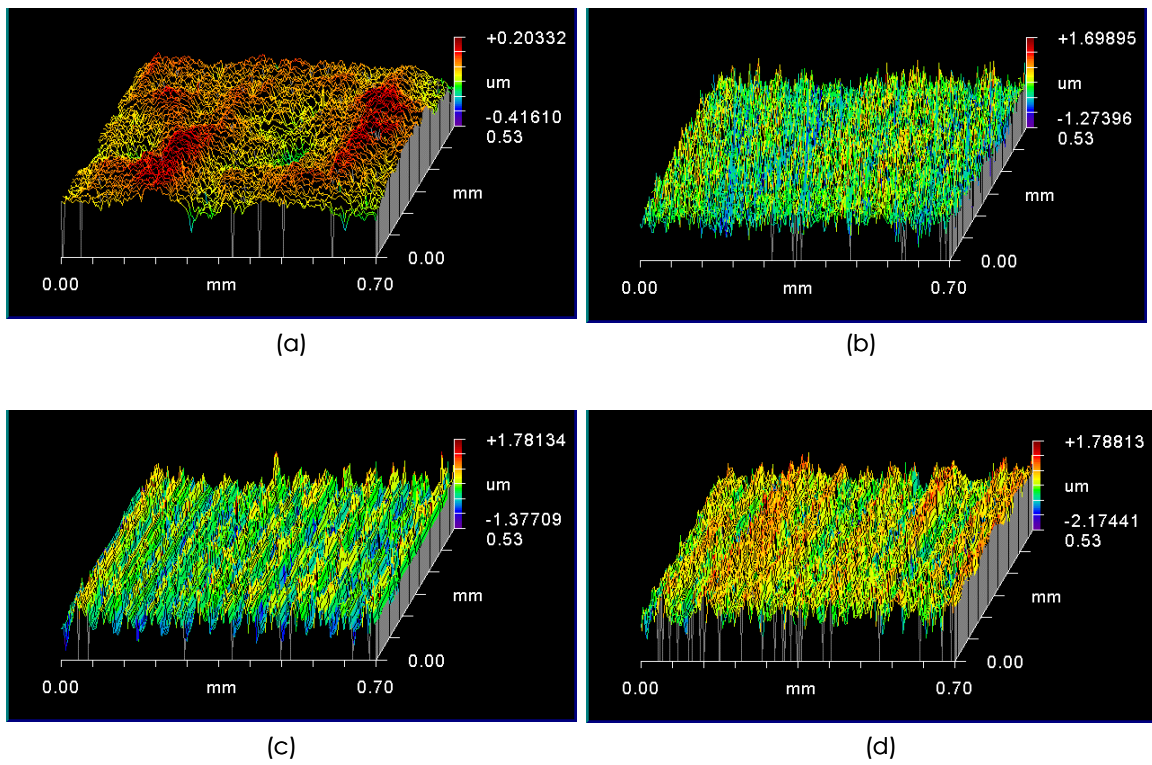


Figure 4.2: Topographic Maps of (a) IF, (b) HN, (c) HT, and (d) GD

The overall surface textures are evident in these images. The HT surface shows the very ordered, periodic peaks and valleys typical of a turning process with a very well defined texture direction or lay. The GD surface shows a similar texture direction, but its peaks and valleys appear more random in height, depth, and spacing. Similarly, the HN sample shows two such distinct texture directions separated by the obvious cross hatch angle ($\sim 30^\circ$) that exemplifies honed finishing while each texture direction lacks consistent height and spacing. Alternately, the IF surface has considerably smaller height variation while displaying no discernable texture direction, hence its isotropic moniker. While these broad descriptions are helpful in seeing qualitative differences in the surfaces, it is necessary to quantify these differences in order to compare their effects on frictional response. The surface parameters first mentioned in Chapter 2 were evaluated for each surface and the results follow.

4.2 Three Dimensional Surface Parameter Results

Amplitude Parameters

While each surface type has a different shape and overall texture, amplitude parameters illustrate the general departure of each surface from a perfectly flat plane. The root mean square roughness (S_q) quantifies the average asperity height in a surface map, but alone gives no information about the shape of a typical asperity. The RMS deviation

parameter is governed by the following continuous and discrete equations:

$$S_q = \sqrt{\frac{1}{l_x l_y} \int_0^{l_y} \int_0^{l_x} \eta^2(x, y) dx dy} = \sqrt{\frac{1}{MN} \sum_{j=1}^N \sum_{i=1}^M \eta^2(x_i, y_j)} \quad (1)$$

where l_x and l_y are the length and width of the sampling area respectively [5]. The skewness (S_{sk}) lends a little more information about each surface by identifying the dominance of either peaks ($S_{sk} > 0$) or valleys ($S_{sk} < 0$). This parameter is defined as the following:

$$S_{sk} = \frac{1}{S_q^3} \int_{-\infty}^{\infty} \int_{-\infty}^{\infty} \eta^3(x, y) p(\eta) p(\eta) y = \frac{1}{MNS_q^3} \sum_{j=1}^N \sum_{i=1}^M \eta^3(x_i, y_j) \quad (2)$$

where $p(\eta)$ is the probability density function of the residual surface $\eta(x, y)$ [5]. The residual surface is the true surface minus the long waviness of the surface; the surface fit to its mean plane. Table 4.1 contains the mean and standard deviation of the amplitude parameters for each surface measured.

Table 4.1: Amplitude Parameters

Mean (St. Dev.)	IF	HN	HT	GD
S_q (μm)	0.066 (0.008)	0.26 (0.048)	0.32 (0.042)	0.52 (0.066)
S_{sk}	-1.60 (0.54)	-0.06 (0.27)	0.29 (0.24)	-0.52 (0.23)

Notice that the surfaces have been ordered in ascending RMS roughness in the table and this convention will continue throughout this chapter. These results lend to the conclusions that the IF surface is the

smoothest overall and the most consistent from sample to sample while the GD surface is roughest and least repeatable. The respective roughness of HN and HT lie between these two with the former being slightly smoother than the latter. According to Thomas [4], abraded surfaces such as GD, HN, and IF exhibit negative skewness whereas HT, a cutting process, will have skewness values nearing zero. The data collected here supports those claims although the variation in the values is slightly larger than expected suggesting a more random nature to skewness characteristics in actual finished surfaces.

Spatial Parameters

To compute the values of the three-dimensional spatial parameters for the surfaces in question, the areal autocorrelation function (AACF) along with areal power spectral density (APSD) of each surface must first be computed. These calculations yield information vital to the calculation of the texture-based parameters and evaluate the dominant surface variation frequencies.

Areal Autocorrelation Function (AACF)

The autocorrelation function describes the dependence of a data point on the other data in a set. For three-dimensional surface analysis an areal ACF is required to associate data in a two-dimensional scan area

with their heights in a third dimension. The AACF is given by the following equations [7]:

$$\begin{aligned} R(\tau_x, \tau_y) &= E[\eta(x, y) \eta(x + \tau_x, y + \tau_y)] \\ &= \lim_{l_x, l_y \rightarrow \infty} \frac{1}{4l_x l_y} \int_{-l_y}^{l_y} \int_{-l_x}^{l_x} \eta(x, y) \eta(x + \tau_x, y + \tau_y) dx dy. \end{aligned} \quad (3)$$

A non-biased discrete estimation of the AACF that is more convenient for numerical computation is evaluated as follows [7]:

$$R(\tau_i, \tau_j) = \frac{1}{(M-i)(N-j)} \sum_{l=1}^{N-j} \sum_{k=1}^{M-i} \eta(x_k, y_l) \eta(x_{k+i}, y_{l+j}) \quad (4)$$

where, $i = 0, 1, \dots, m < M; j = 0, 1, \dots, n < N; \tau_i = i\Delta x; \tau_j = j\Delta y$, $\eta(x, y)$ is the residual surface [37] after a plane is fit to remove the form (longer wavelength and undulations) from the surface data; m and n are the autocorrelation lengths in the x and y directions, respectively.

Statistical confidence decreases as i and j approach M and N , respectively, as fewer data points are available for computation of AACF.

This limitation causes x and y to be limited to $\tau_m = \Delta x M/2$ and $\tau_n = \Delta y N/2$.

The AACF helps to visualize the correlation of surface profile heights in different directions. The decay of correlation will be very slow in the direction of consistent surface height whereas the decay will be very fast in the direction of more random surface height values. If a surface has periodicity, its decay will illustrate that periodicity. Consequently, AACF analysis is used to compute parameters such as texture aspect ratio (S_{tr})

and fastest decay autocorrelation length (S_{al}). The AACF plot for each surface is shown in Figure 4.3.

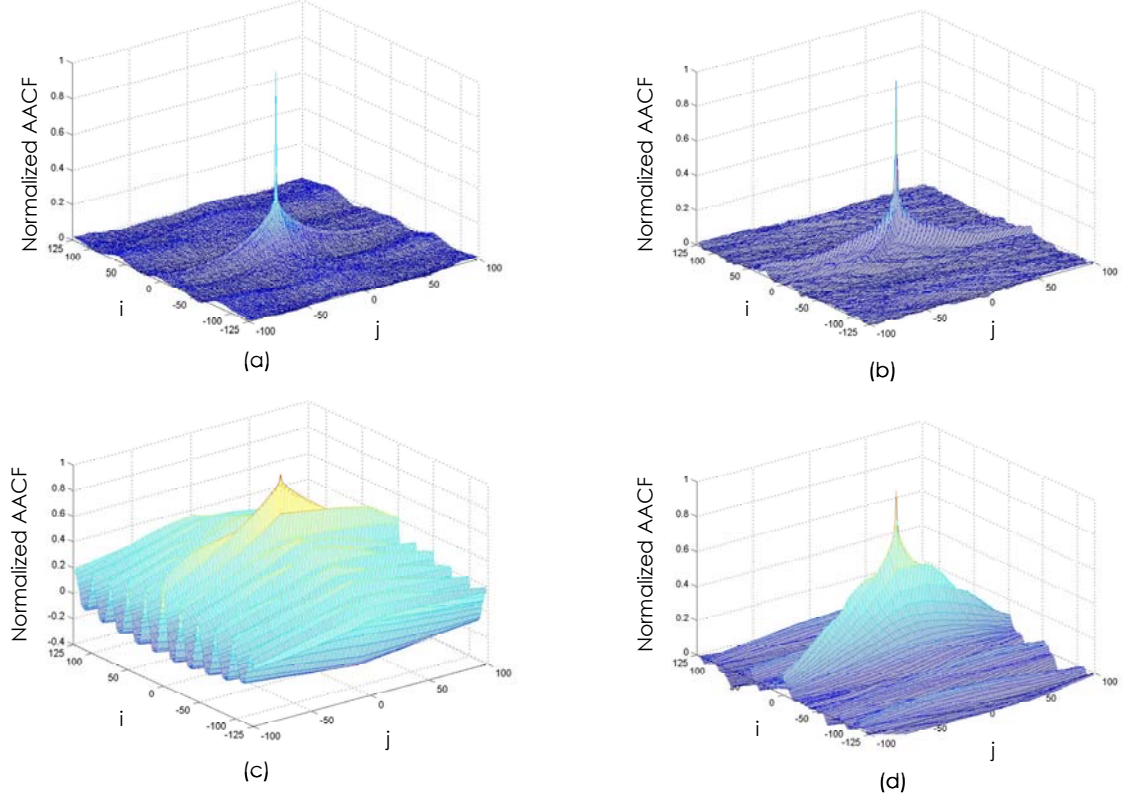


Figure 4.3: AACF plots for (a) IF, (b) HN, (c) HT, and (d) GD

This plot helps to visualize the direction of any correlation exhibited by a surface and will be instrumental in calculating the fastest decay autocorrelation length (S_{al}). It is evident from Figure 4.3(a) that the IF surface has uniform decay in all directions. This suggests no significant correlation in any particular texture direction on the surface itself. This fact supports the isotropic description of this surface and lends credence to the idea that texture direction can be inferred somewhat from the AACF

function. Next, at the opposite end of the correlation spectrum, the HT surface in Figure 4.3(c) shows significant correlation both along the lay direction and across it. This is due to the very consistent depth of the cutting process along each valley and the periodic peak spacing from a constant feed rate during the turning process. The GD surface in Figure 4.3(d), however, shows very slow decay along its lay, but very fast decay across it. This result is expected knowing that the depth of each groove made by this abraded process is consistent along its own depth, but the spacing of those grooves and the depth from groove to groove show no discernable pattern. Finally, in Figure 4.3(b), the HN surface shows a decay pattern similar in shape to the GD surface but much smaller in amplitude and in two distinct directions separated by a specific angle. This result aligns nicely with the crosshatch pattern typical of a honed surface and shows that its grooves are much less consistent in depth than the GD surface and therefore do not correlate as strongly. The specific angle of the honing pattern will be identified later in this chapter using angular spectral density analysis.

Areal Power Spectral Density (APSD)

Areal spectral analysis reveals the dominant frequencies in the texture patterns of a surface. It is used to compute the texture direction

parameter (S_{tr}). For the residual surface $\eta(x,y)$, its continuous and discrete Fourier transforms are given by Eqs.(5) and (6), respectively.

$$F(\varpi_x, \varpi_y) = \int_{-\infty}^{\infty} \int_{-\infty}^{\infty} \eta(x,y) e^{[-j2\pi(\varpi_x x + \varpi_y y)]} dx dy \quad (5)$$

$$F(\varpi_p, \varpi_q) = \sum_{l=1}^{N-1} \sum_{k=1}^{M-1} \eta(x_{k+1}, y_{l+1}) e^{[j2\pi(\frac{p}{M}k + \frac{q}{N}l)]} \quad (6)$$

where ϖ_p and ϖ_q are angular frequencies in two directions as defined below:

$$p = 0, 1, \dots, M-1; q = 0, 1, \dots, N-1;$$

$$\varpi_p = \frac{p}{\Delta x M}, \varpi_q = \frac{q}{\Delta y N}$$

The areal PSD can be implemented by[7]:

$$G(\varpi_p, \varpi_q) = F(\varpi_p, \varpi_q) F^*(\varpi_p, \varpi_q) \quad (7)$$

where ‘*’ denotes complex conjugate.

Anisotropic surfaces have power densities that run perpendicular to their lay patterns. If the lay pattern is highly ordered, the power will be concentrated at specific frequency intervals and harmonics thereof. In a random or isotropic surface, no discernable texture pattern exists and power is concentrated at the origin with almost instant decay in all directions. The APSD is most useful in computing the texture direction (S_{td}) parameter. Figure 4.5 shows the APSD plots for each surface. If a lay pattern exists, the power should be concentrated perpendicular to the

lay direction and if the surface in question is strongly periodic, the power will be further concentrated at specific frequencies. In Figure 4.4(a) the IF surface's power spectrum is very dense at the origin and practically zero everywhere else.

This further supports the isotropic nature of this surface because a surface without any discernable pattern will not concentrate power in a particular direction or period. Figure 4.4(c) illustrates power concentrated at a specific frequency outward from the origin in the HT surface. This result matches expectations because the HT surface is highly ordered both along and across its lay pattern. Figure 4.4(b) shows power concentrated perpendicular to the lay pattern of the GD surface, but without the further concentration at specific points across its lay. This, too, is expected knowing the presence of a specific texture direction but absence of periodicity resulting from the grinding process. Finally, the HN surface in Figure 4.4(b) shows very similar power concentration to the GD surface, but perpendicular to two different texture directions. Again, this illustrates the presence of two surface texture directions separated by a specific and consistent angle.

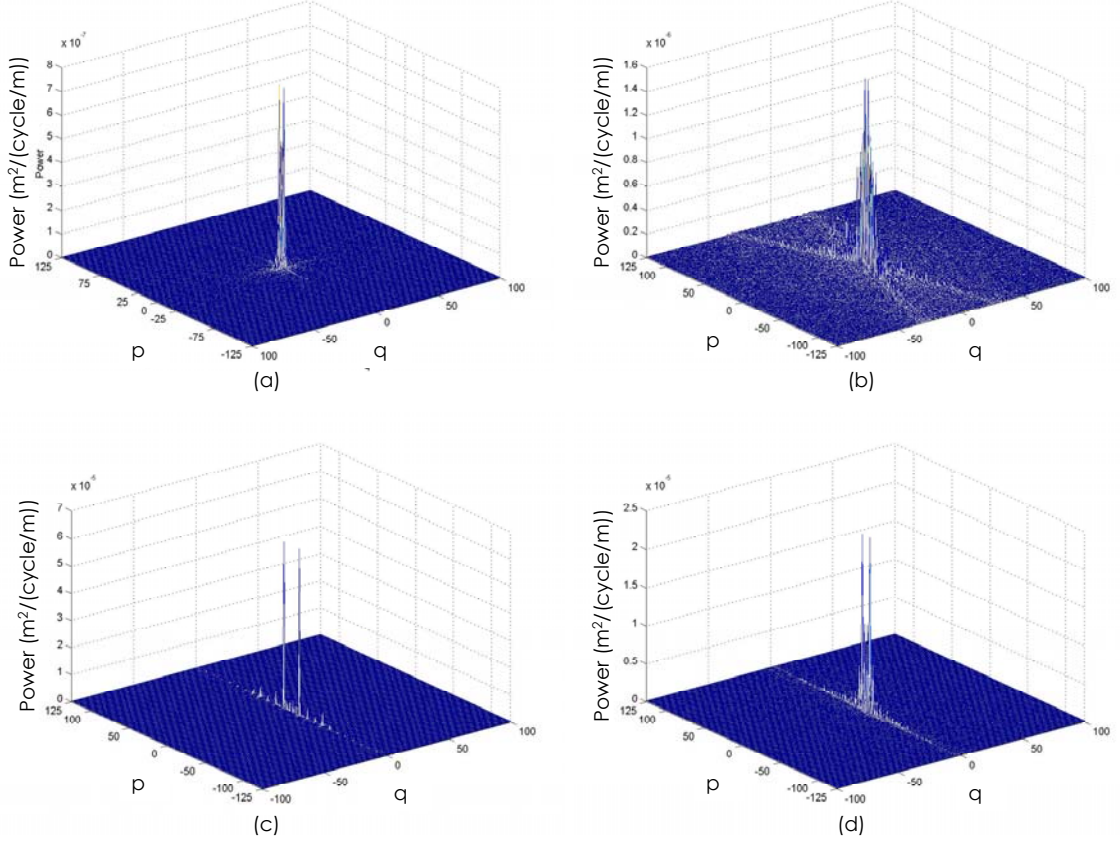


Figure 4.4: APSD plots for (a) IF, (b) HN, (c) HT, and (d) GD

The texture direction was found by plotting the angular spectrum of each surface's APSD plot. S_{td} is computed as follows [7]:

$$\begin{aligned}
 S_{td} &= -\beta, \beta \leq \pi/2 \\
 &= \pi - \beta, \pi/2 < \beta \leq \pi
 \end{aligned} \tag{8}$$

where β = value of θ at which $G_\alpha(\theta)$ is maximum. $G_\alpha(\theta)$ is the angular spectrum derived from APSD by integrating the spectral energy radially between 0 and 179 degrees.

$$\left. \begin{aligned} G_a(\theta) &= \int_0^{R(\theta)} G(\theta(r)) dr \\ R(\theta) &= \frac{1}{2} [(\Delta x \cos \theta)^2 + (\Delta y \sin \theta)^2]^{-1/2} \\ 0 \leq \theta &\leq 179 \end{aligned} \right\} \quad (9)$$

Recall that since the reference frame can be determined arbitrarily, it is defined here by Figure 4.5.

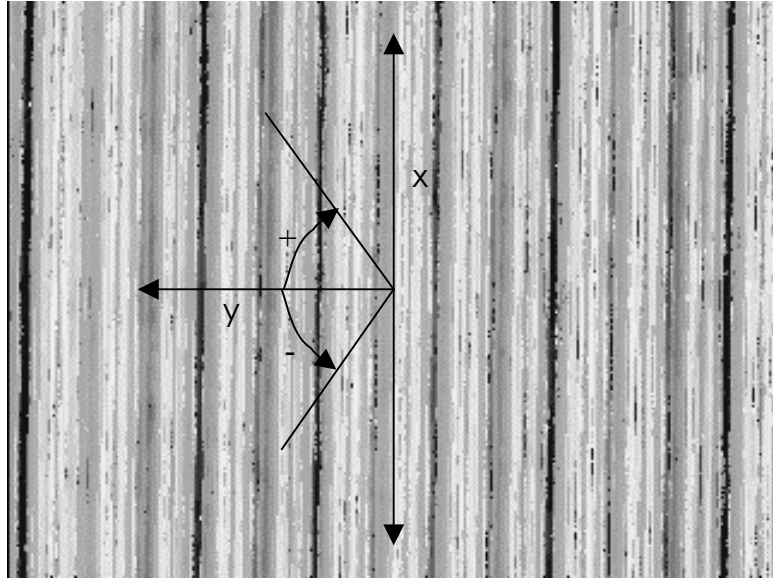


Figure 4.5: Texture Direction Defined

The maximum power will occur at the angle from the y-axis that the texture lies along. The angular spectrum plots for each surface can be seen in Figure 4.6. The IF surface in Figure 4.6(a) has no dominant angular dependency and the peaks that are seen are of extremely small magnitude. This further proves the lack of texture in the IF surface. The HT and GD surfaces in Figure 4.6(c) and (d) show obvious dominant texture direction perpendicular to the y-axis, which is consistent with their AACF

data, giving them a texture direction of ninety degrees. The nominal acute crosshatch angle of the HN surface is thirty degrees. Owing to the orientation of the axes, the texture direction here should reflect the obtuse angle supplementary to thirty degrees: one hundred fifty degrees. The texture direction of this surface then is seventy-five degrees in each direction from the y-axis.

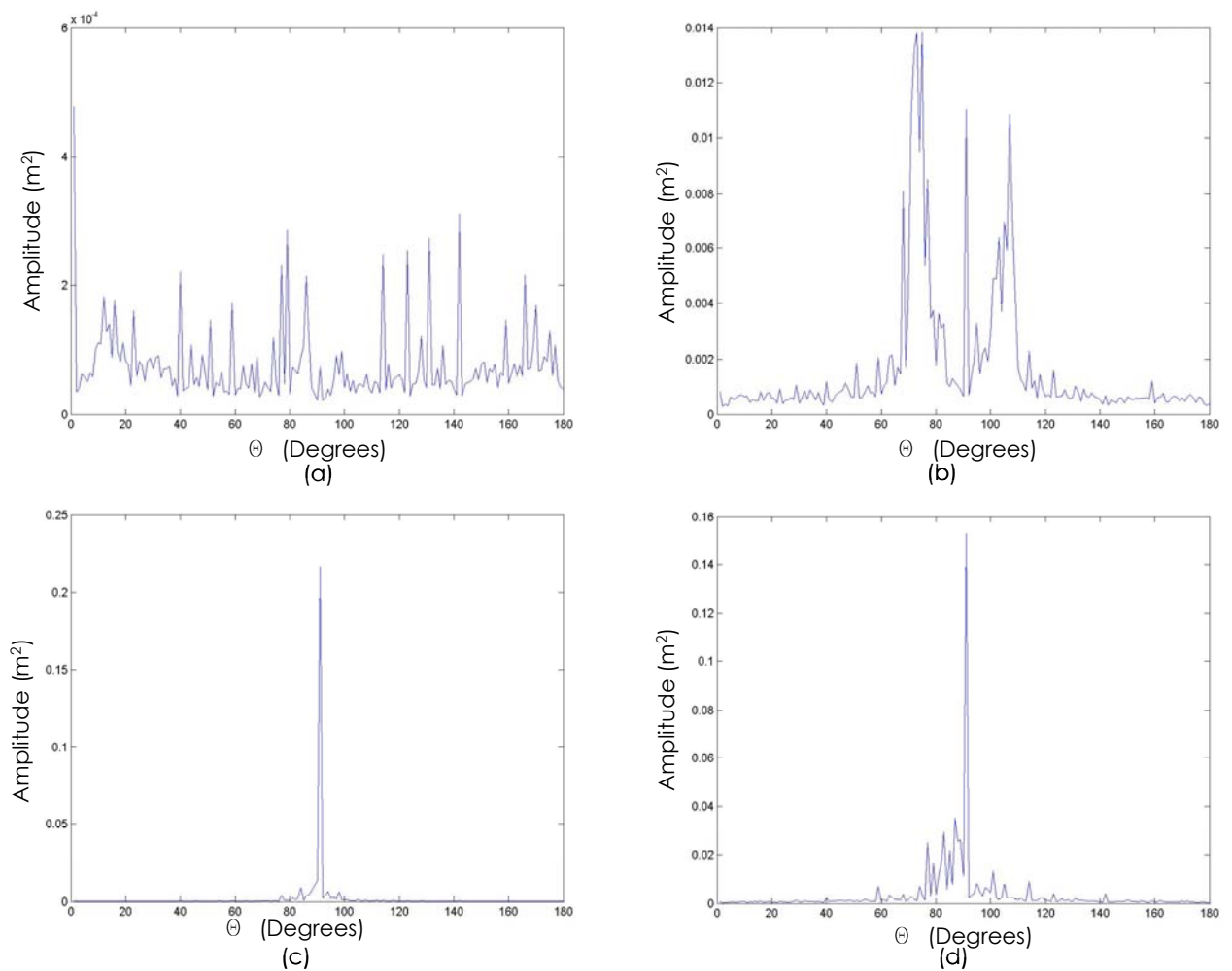


Figure 4.6: Angular Spectra for (a) IF, (b) HN, (c) HT, and (d) GD

With the AACF and APSD information in hand, the spatial parameters of each surface can be computed. The spatial parameters of interest are the fastest decay autocorrelation length (S_{al}), density of summits (S_{ds}), texture aspect ratio (S_{tr}), and texture direction (S_{td}). Table 4.2 lists the values of each parameter and its standard deviation for each surface.

Table 4.2: Spatial Parameters

Mean (St. Dev.)	IF	HN	HT	GD
S_{al} (μm)	43.84 (13.03)	8.79 (4.83)	44.79 (19.86)	18.21 (11.95)
S_{ds} (/mm ²)	72.97 (10.45)	2,129.68 (52.55)	92.25 (22.11)	636.40 (35.09)
S_{tr}	0.68 (0.12)	0.27 (0.13)	0.19 (0.09)	0.10 (0.07)
S_{td}	none	-75 °, 75 °	90°	90°

As discussed in Chapter 2, the fastest decay autocorrelation length is an indicator of the waviness character of a surface. It is used here to identify an appropriate window in which to calculate the density of summits (S_{ds}). S_{al} can be computed using [7]

$$S_{al} = \min(\sqrt{T_x^2 + T_y^2}, \bar{R}(T_x, T_y)) \leq 0.2. \quad (10)$$

From Table 4.2 IF and HT have similar S_{al} values due to their low frequency dominated surfaces. The IF surface is low frequency dominated because its roughness is very small compared to changes in its surface height over large areas, whereas the HT surface has a definite low frequency periodic

nature which overwhelms its significant roughness. In either case, it is important to have a large window in which to count summits so that only relative global peaks likely to behave as true summits will be counted. For the HN surface and to a lesser degree the GD surface, the high frequency roughness dominates the longer wavelength changes in surface height when compared with IF and HT. For this reason, a relatively smaller window is necessary for counting summits so that no true summits are missed in these more high frequency based surfaces. This leads directly to the density of summits (S_{ds}) calculation. Its computation follows [7]:

$$S_{ds} = \frac{\text{Number of Summits}}{(M-1)(N-1)\Delta x \Delta y} \quad (11)$$

The IF surface has the fewest summits per square millimeter on average followed closely by the HT surface. Keep in mind that S_{ds} makes no suggestion as to the shape of each peak, but only counts the peaks themselves. The GD surface has almost ten times the number of peaks per square millimeter of IF, and the HN surface has more than three times that of GD. Finally, the texture aspect ratio of each surface yields another insight into the degree of isotropy of a surface. A value less than 0.5 will tend to identify an anisotropic surface while a value greater than 0.5 will likely point to isotropic characteristics. It is defined as follows:

$$S_{tr} = \frac{\text{Distance that the normalised AACF decays fastest to 0.2 in any direction}}{\text{Distance that the normalised AACF decays slowest to 0.2 in any direction}} \quad (12)$$

As expected, the only surface to be found isotropic is the IF surface while each of HN, HT, and GD show anisotropic nature. Little can be said regarding the meaning of more or less isotropic behavior except that the surfaces that earlier displayed a definite texture direction are validated as being anisotropic in nature and vice-versa.

Hybrid Parameter

The only hybrid parameter of interest in this work is the RMS Slope ($S_{\Delta q}$). As discussed in Chapter 2, $S_{\Delta q}$ characterizes the root mean slope of the surface. This lends itself beautifully to further clarifying the density of summits calculation made earlier. A highly sloping surface will tend to have sharper peaks and valleys while a surface having smaller slope will have rounder more gently sloping asperities. The root mean square slope within a sampling area is computed by [7]:

$$\rho_{ij} = \left[\left(\frac{\eta(x_i, y_j) - \eta(x_{i-1}, y_j)}{\Delta x} \right)^2 + \left(\frac{\eta(x_i, y_j) - \eta(x_i, y_{j-1})}{\Delta y} \right)^2 \right]^{1/2} \quad (13)$$

$$S_{\Delta q} = \left(\frac{\sum_{j=2}^N \sum_{i=2}^M \rho_{ij}^2}{(M-1)(N-1)} \right)^{0.5} \quad (14)$$

The $S_{\Delta q}$ values of each surface can be seen in Table 4.3.

Table 4.3: Hybrid Parameter

Mean (St. Dev.)	IF	HN	HT	GD
$S_{\Delta q}$ (rad)	0.03 (0.007)	0.18 (0.037)	0.15 (0.021)	0.26 (0.027)

The values in Table 4.3 fit very well to what would be intuitively expected given the previous characterizations. The IF surface has, by far, the smallest slope due to its very smooth nature and isotropic texture. Its peaks are then very rounded and gently rising and falling in all directions. The slopes of the HN and HT surfaces and therefore the shape of their respective asperities are very similar. Because the roughness of the HT surface is larger than that of HN, its peaks are likely taller than the honed surface's, but the HN surface has drastically more peaks per unit area than its hard-turned counterpart. Finally, the GD surface has the sharpest slopes of any surface and also the tallest according to its roughness parameter. This validates its consideration as the roughest overall.

4.3 Summary

This chapter focused on the initial qualitative as well as later quantitative characterization of each surface under investigation. As expected, the IF surface proved to be the smoothest, most isotropic, and gently sloping of the finishes in question. Alternately, the GD surface is the roughest surface while it retains some definitive texture direction. The HN

surface is slightly smoother than the HT surface, but has drastically more summits per unit area. These two finishes share a common sharpness of asperity and the interaction of these parameters with one another is sure to be of some interest. The HT and HN finishes both have a definite texture direction with the HT texture being very regular and periodic across the lay. These parameters are necessary to evaluate the surfaces in an unambiguous way so that differences between them can be cited as explanations of trends in the coefficient of friction data to follow. They will be the necessary and hopefully sufficient link between a surface's makeup and its functionality and are therefore vital to the scope of this work.

Chapter 5

Results and Discussion

In the previous chapter, the different three-dimensional surface parameters for each surface type used in this study were calculated. These data show a significant difference between the topographic character of some of the surfaces and identify similarities among them. To realize the goal of this work, the coefficient of rolling/sliding friction of each surface must be found and then compared to its respective surface parameters. Using the friction testing rig detailed in Chapter 3, an experiment was performed that sought to uncover this missing information. The details of this experiment and the results obtained from it are the subject of this chapter.

5.1 Experimental Design

The coefficient of rolling/sliding friction under line contact conditions is generally influenced by a number of factors such as lubrication, surface texture, normal load, and slide-to-roll ratio. In this thesis, the effects of surface type and slide-to-roll ratio encountered under typical roller bearing operating conditions were investigated. Each of the four surfaces detailed in Chapter 4 were tested at four different slide-to-

roll ratios. The slide-to-roll ratio of two surfaces in rolling/sliding contact is calculated using equation (1)

$$SR = \frac{U_2 - U_1}{\left(\frac{U_1 + U_2}{2}\right)} \quad (1)$$

where U_1 and U_2 are the surface speeds. Here, since the samples share a common radius, the surface speed is determined by the rotational speed of the samples. The speed of the sample which the torque transducer monitors was fixed at 1000 RPM while the other sample's speed was set to 905, 818, 739, and 667 RPM for 0.1, 0.2, 0.3, and 0.4 slide-to-roll ratios, respectively. Table 5.1 shows the factors and their levels for this experiment.

Table 5.1. Factors and Their Levels in Experiment

Type of Surface	Slide-to-Roll Ratios
Ground (GD)	0.1
Honed (HN)	0.2
Hard Turned (HT)	0.3
Isotropic Finished (IF)	0.4

The output of interest in this experiment was the mean coefficient of rolling/sliding friction as a function of the surface type.

Although normal load is a factor that affects the coefficient of rolling/sliding friction, its effect was not studied in this experimental work. Under normal operating conditions, a roller element bearing can often be placed under loads on the order of thousands of Newtons. The necessary

stiffness and safety precautions that these loads would require are both expensive to produce and require specific facilities to manage. Due to limited resources such as these in the design and construction of the friction testing rig, its robustness is limited and therefore the loads that it can apply lie in a relatively small range; it has a maximum load capability of 420 Newtons (~95 lbs) from the compressed air facilities available. A major effect of load in lubricated rolling/sliding contact is on the fluid film thickness. The lubrication conditions will be discussed in greater detail later in this chapter, but for now it is important to note that drastic changes in load are required to significantly change the fluid film thickness [39]. Because load changes on the order of thousands of Newtons are not possible in this experimental setup, normal load was kept constant throughout the experiment and its effect on coefficient of rolling/sliding friction cannot, therefore, be determined.

Likewise, lubrication is an important factor in the determination of the coefficient of rolling/sliding friction. SAE 5W-30 motor oil was used as the lubricant in all cases and because the load was kept constant, the actual lubrication conditions only change with the speed of the surfaces [19]. To characterize the lubricant, the limiting low shear viscosity was determined by falling body viscometry [40, 41]. The change in limiting low shear viscosity, μ_s , as a function of pressure at 20°C is given in Table 5.2.

These values are used to determine the pressure-viscosity coefficient given by equations (2) and (3).

Table 5.2. Pressure-viscosity relationship

Pressure (MPa)	Limiting Low Shear Viscosity, μ_s (Pa.s)
0	0.11
50	0.382
100	1.064
200	6.22
250	13.96
300	29.8

$$\alpha^* = \left(\int_0^\infty \frac{\mu_s(0)}{\mu(p)} dp \right)^{-1} = 23.0 \text{ GPa}^{-1} \quad (2)$$

$$\alpha_o = \left. \frac{d \ln(\mu_s)}{dp} \right|_{p=0} = 27.1 \text{ GPa}^{-1} \quad (3)$$

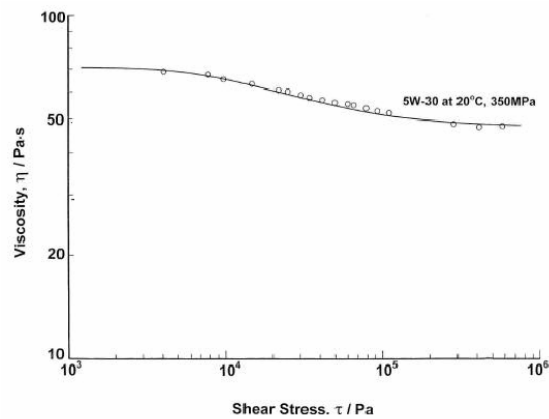


Figure 5.1: Flow Curve for SAE 5W-30

The change in viscosity of the lubricant as a function of shear stress is illustrated in Figure 5.1. Measurements were made using a pressurized Couette rheometer. The figure shows the performance of the lubricant as

a function of shear stress under constant pressure (350 MPa) and temperature (20°C). It is clear from the figure that the lubricant displays shear thinning behavior and a second Newtonian response. Shear thinning is evident in the central portion of the curve in Figure 5.1 where the viscosity drops as shear stress is increased from 10^4 to 10^5 Pa. The first Newtonian response is seen at the far left of Figure 5.1 where viscosity is constant as shear stress increases to about 10^4 Pa and the second Newtonian response is evident as shear stress approaches 10^6 Pa.

To determine the film thickness in the experiment, a smooth elastohydrodynamic lubrication (EHL) line contact estimation by Dowson et al. [39] was used. The formulae are non-dimensional and yield the non-dimensional central film thickness, (h_o^*) , and the minimum film thickness (h_m^*) for flooded contact. These equations are as follows:

$$h_o^* = 1.654U^{0.7}G^{0.54}W^{-0.13} \quad (4)$$

$$h_m^* = 1.93U^{0.69}G^{0.56}W^{-0.1}. \quad (5)$$

As stated above, these equations are dependent on fully flooded boundary conditions. In order for this to be accurate, surplus lubricant must always be available at the inlet. In this experiment, the lubricant was applied drop-by-drop (~2 Hz) from a reservoir directly above the line of contact. This creates a more starved lubrication situation that eliminates re-circulation of the oil at the converging gap inlet and creates a zero reverse flow boundary condition [42]. Under fully flooded lubrication

conditions, a very large volume of fluid is being forced into the converging gap where it cannot all possibly fit. Some of this excess volume will flow back against the direction of the surfaces and be subsequently drawn back into the gap. This vortex type flow is not present if there is just enough lubricant at the gap to create an EHL film but not enough to create reverse flow in the excess fluid. Therefore, there is no recirculation of lubricant at the inlet in a zero reverse flow boundary condition. This partially starved lubrication regime is typical of roller bearings.

Dowson et al. [42] showed that, in pure rolling, elastohydrodynamic contacts receive only seventy percent of the predicted fully flooded film thickness values when the zero reverse flow boundary is observed. For pure sliding, the film thicknesses are reduced to only forty six percent of the predicted values. The experiment conducted here involves rolling/sliding contact that will also account for some variation in the predicted film thickness.

The predicted minimum smooth film thickness for fully flooded contact from equation (5) varies from $2.7\mu\text{m}$ for the 0.1 slide-to-roll ratio case to $2.3\mu\text{m}$ for slide-to-roll of 0.4. This difference is due to the slower combined surface speed in the 0.4 case compared to 0.1. EHL film development is heavily dependent on surface speed since it is the forcing of lubricant into a converging gap at high speed that builds up lubricant

film pressure. Taking into account the zero reverse flow boundary condition and the rolling/sliding nature of the contact, the actual minimum film thickness is on the order of $1\mu\text{m}$. From the roughness data in Chapter 4, this indicates a mixed lubrication regime for three of the surfaces (GD, HT, HN) since the composite root mean square deviation of the asperities is very near half of the film thickness [19]. The IF surface, on the other hand, has roughness a full order of a magnitude smaller than the film thickness estimation and hence operates under a full EHL lubrication regime[19].

The samples used in this experiment were provided by The Timken Company specifically for this work. Each sample disc is $76.2\text{mm} \pm 2.54\text{mm}$ in diameter, $25.4\text{mm} \pm 0.25\text{mm}$ thick, and has an $18.9\text{mm} \pm 25\mu\text{m}$ axial hole through its center. Because roundness errors had to be absolutely minimal, tight tolerances were assigned for concentricity ($\pm 12\mu\text{m}$) and sizing of the inner diameter. The samples used here are AISI 52100 high carbon steel, a material prominent in the bearing industry. They were through hardened to 60-62 Rockwell C and then finished on their outer diameter by one of the prescribed processes discussed herein. Upon their receipt, each sample was press-fitted to a shaft that would support the sample during its testing.

The modulus of elasticity (E) for the samples is 210 GPa. The Poisson's ratio is 0.3. Converting the sample sizes to metric units for

contact calculations, the diameter is 76.2mm and the length of the line of contact is 25.4mm. The maximum Hertzian contact pressure and contact ellipse semi-minor axis are given in Table 5.3. Table 5.4 shows the plasticity index (Ψ) for the surfaces being evaluated (as defined by Mikic [43]) as a function of surface geometry (rms slope, $S_{\Delta q}$) and material properties.

$$\psi = \frac{E'S_{\Delta q}}{H} \quad (6)$$

where,

$$E' = \frac{1}{2 \left(\frac{1-\nu^2}{E} \right)}$$

Table 5.3. Hertzian Contact Details

Normal Load (N)	Maximum Hertzian Contact Pressure (MPa)	Contact Semi-minor Axis (mm)
334	158.98	0.052

Table 5.4. Plasticity Indices for Precision Finished Surfaces

Surface	RMS Slope ($S_{\Delta q}$)	Plasticity Index (ψ)
GD	0.26	4.67
HN	0.18	3.17
HT	0.15	2.72
IF	0.04	0.63

The values of plasticity indices exceed unity in all cases but for IF indicating that the asperities are deformed plastically in all cases except

for the IF surface. The asperities deform elastically in the case of the IF surface.

Because only four of each surface type were available for this experiment, a method to collect sufficient data for analysis from a small sample set was devised. Prior to use in any test, each sample was characterized using the white light interferometry system detailed in Chapter 4. Then, after testing of each sample pair was completed, they were placed back in the characterization system to view any changes in the surfaces as a result of the testing process. For example, the grayscale images and three-dimensional topography of the same point on an HT surface before and after testing are seen in Figure 5.2. The surface parameters of interest from before and after tests for the same HT surface are listed in Table 5.5.

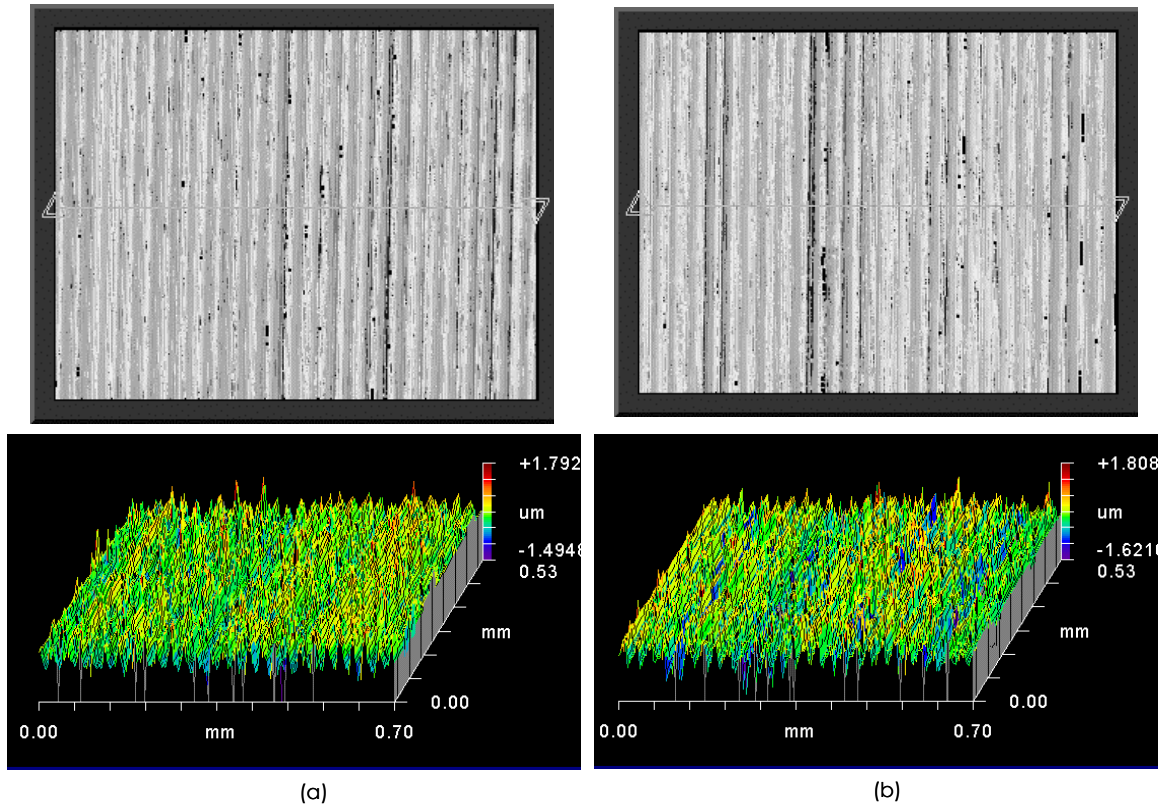


Figure 5.2: Grayscale and topography of an HT surface (a) before and (b) after testing

Table 5.5: Surface Parameters Pre- and Post-testing for HT surface

	S_q	S_{dq}	S_{ds}
Pre-testing	.332 μ m	0.180	94.98
Post-testing	.370 μ m	0.192	89.53

Although the plasticity indices indicate that there is plastic deformation of some asperities in the rougher surfaces, it is isolated mainly in the tallest asperities and does not significantly affect the surface parameters calculated for each surface. This was validated using a t-distribution test of the parameter values of each surface before and after its use and proved that the variation of those parameters are no greater as a result of use in the experiment than the normal variation of the

parameters at different locations on a surface. This suggests that the low loads of this experiment do not mar the surfaces considerably and therefore each surface can be used at least for the duration of this experiment without significant changes in its characteristics.

Based on this evidence, for each sample pair loaded into the rig, a randomly ordered sequence of slide-to-roll ratios was administered under a constant load. The order in which the surface pairs were loaded into the rig was also randomized. Each piece of data collected consisted of ten seconds of 1000Hz sampling of the normal load and torque under a given slide-to-roll ratio. Each slide-to-roll ratio appeared five (5) times for a given surface pair resulting in twenty (20) total data files for each surface pair. The exact sequence of the experimental design can be seen in Appendix B. To avoid any thermal effects in the lubricant, for every two minutes of friction testing, the samples were given five minutes to cool while still being fed fresh oil at room temperature. At the beginning of each rest phase, the surfaces were touched by hand to detect significant heat buildup. This qualitative inspection showed that no sample in any test exhibited any significant heating. The surfaces were never hot to the touch and could be handled at all times without any discomfort whatsoever. This is likely a result, again, of the gentle loading conditions relative to other bearing applications and the transport of heat away

from the surfaces by the lubricant as it was replaced by room temperature oil.

Although great care was taken to eliminate runout errors in the testing rig and the surface sample pairs it can never be eliminated entirely. The total runout of the samples used in this study is less than $25\mu\text{m}$. As a result, a cyclic variation in the load and torque signals was expected and observed. Since the rotational frequency of the shaft on which the torque is measure is fixed at 16.667 Hz (1000RPM), filtration of this predictable error was easily implemented. Figure 5.3 shows a power spectral density plot for the load signal of a typical test run. The major peak is rather wide and centered over approximately 17Hz. The smaller peaks that follow at higher frequencies appear to be harmonics of the principle frequency in the signal.

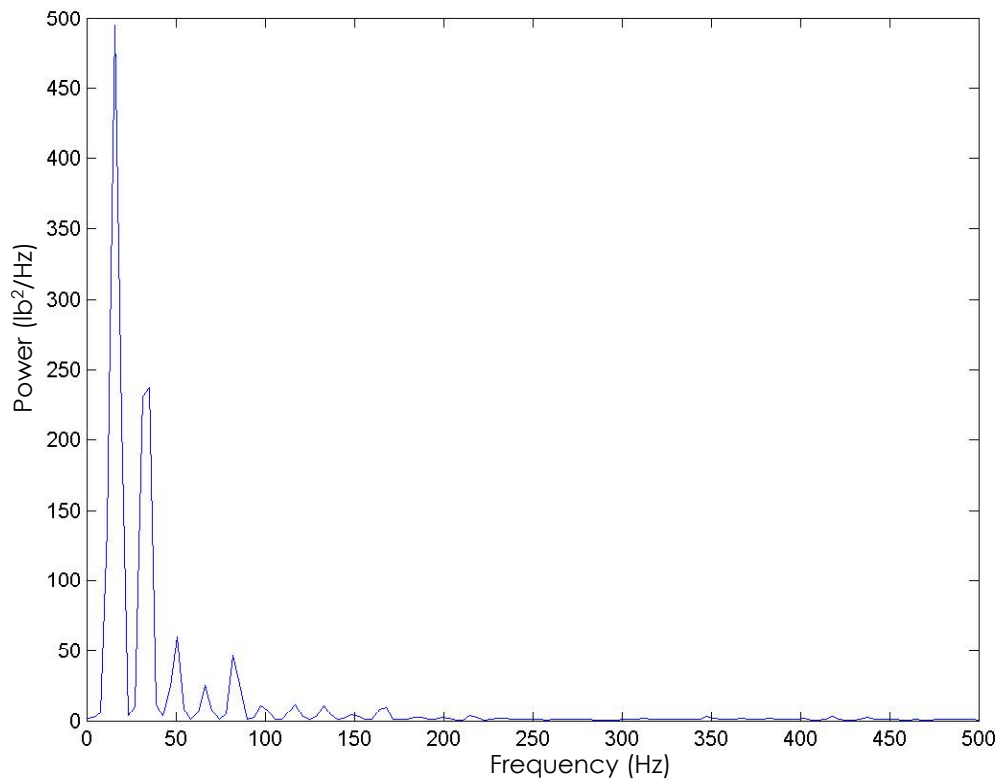


Figure 5.3: PSD Plot for Typical Load Signal

A low-pass butterworth filter was applied at a cut-off frequency of 15 Hz to both the load and torque raw data. Figure 5.4 shows the result of this filtration on the raw data collected during a 0.1 slide-to-roll ratio test of an HN surface for example. With the reduction of this cyclic noise, the signals become more consistent without changing their mean. The MATLAB code used to filter the data can be seen in Appendix A.

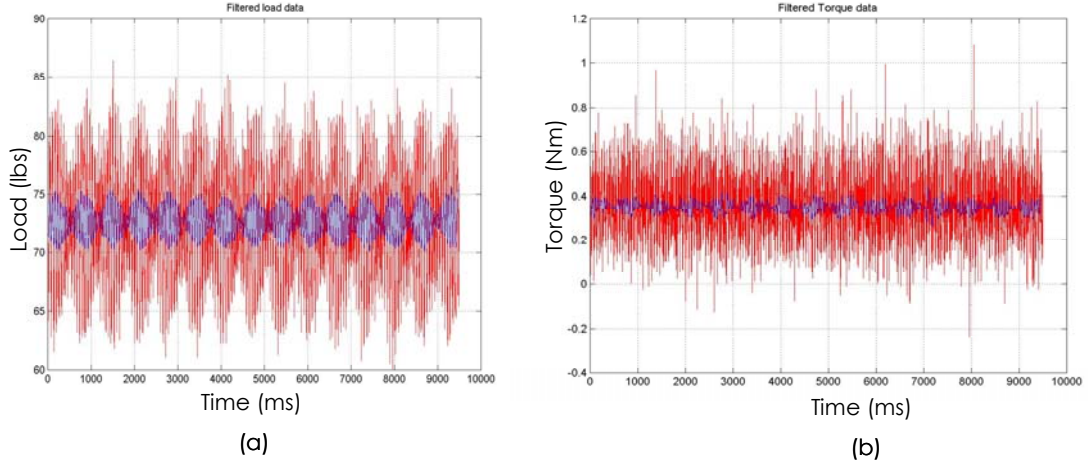


Figure 5.4: Filtered Load (a) and Torque (b) Data for 0.1 S/R HN Surface (Raw Signal in Red, Filtered Signal in Blue)

Once each piece of data was filtered as described above, the coefficient of rolling/sliding friction was calculated as a function of time. The coefficient of friction is computed as:

$$\mu(t) = \frac{T(t)}{F(t) \times r} \quad (7)$$

where, μ is the coefficient of friction, T equals the torque due to friction, F represents the normal load, r is the radius of the disc, and t is time. The mean value of each sample pair's coefficient of rolling/sliding friction was then recorded. After both pairs of each surface had been tested, a total of ten (10) means at each slide-to-roll ratio for each surface were available for analysis. The full list of these means can be seen in Appendix B. In the next section, the results of the friction tests will be analyzed and possible explanations will be postulated.

5.2 Experimental Results

The means and standard deviations of the collected coefficient of friction data are plotted in Figure 5.5. It is obvious that surface type has an effect on the friction response. As seen in the figure, the GD surface yields the highest coefficient of friction while the IF surface yields the lowest. The slide-to-roll ratio also affects friction. The slope of the GD surface plot is quite steep compared to the nearly flat line of the IF surface as slide-to-roll ratio increases. Also evident in the figure is that the HT and HN surfaces share very similar coefficients of friction and also nearly identical slopes with increases in sliding. Certainly these trends in the data are worthy of analysis. First, an ANOVA analysis was performed to identify the levels of the factor effects then correlation between certain three-dimensional surface parameters and the coefficient of rolling/sliding friction were explored.

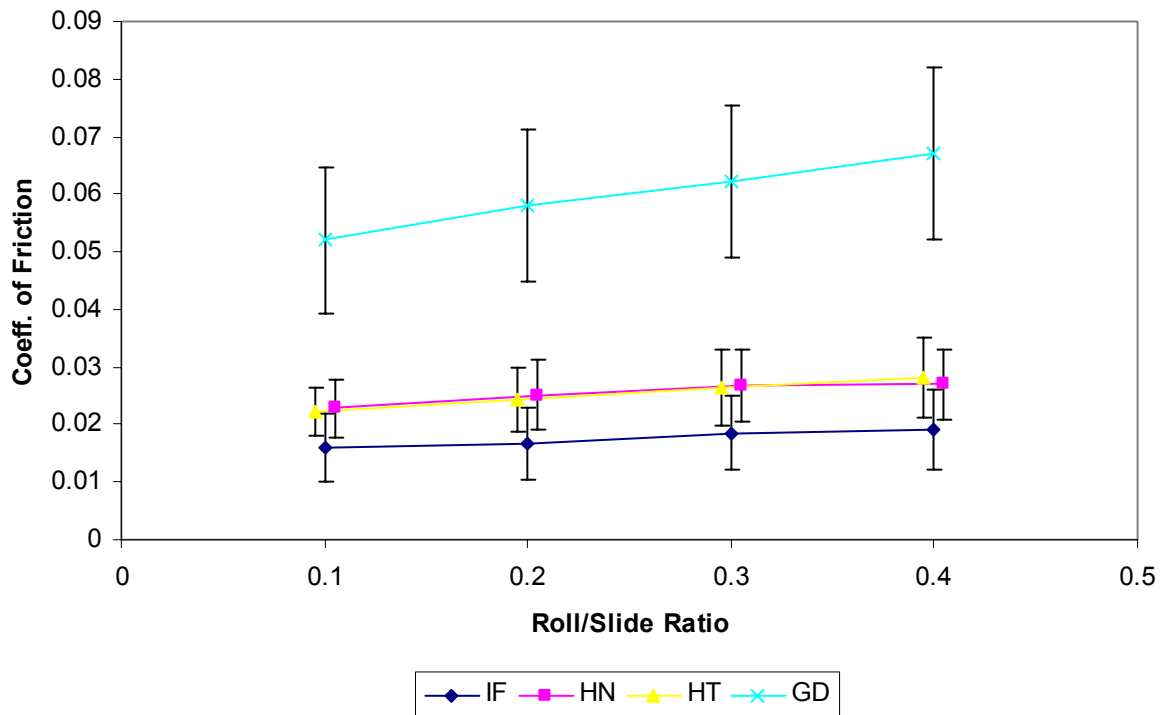


Figure 5.5. Coefficient of Friction as a Function of Slide-to-Roll Ratio and Surface Type (Normal Load=334N)

The ANOVA analysis shows that the main effects of surface type and slide-to-roll ratio on the coefficient of rolling/sliding friction are statistically significant at an α level of 5%. The surface type effects will be discussed first and the slide-to-roll ratio effects will be addressed subsequently. The main effect of surface type yielded the highest mean value of the coefficient of rolling/sliding friction for all slide-to-roll ratios combined for the GD surface and the lowest mean value for the IF surface (Figure 5.6). The coefficient of friction decreases by about 70% from the GD surface to the IF surface while the HT and HN surfaces lie between. The HT surface showed a slightly lower average friction

coefficient than the HN surface, but the difference is only around 1%. The slide-to-roll ratio main effects show a nearly linear increase in coefficient of friction as slide-to-roll ratio rises from 0.1 to 0.4. These results are congruent with what is expected from the visual representation of the data in Figure 5.5.

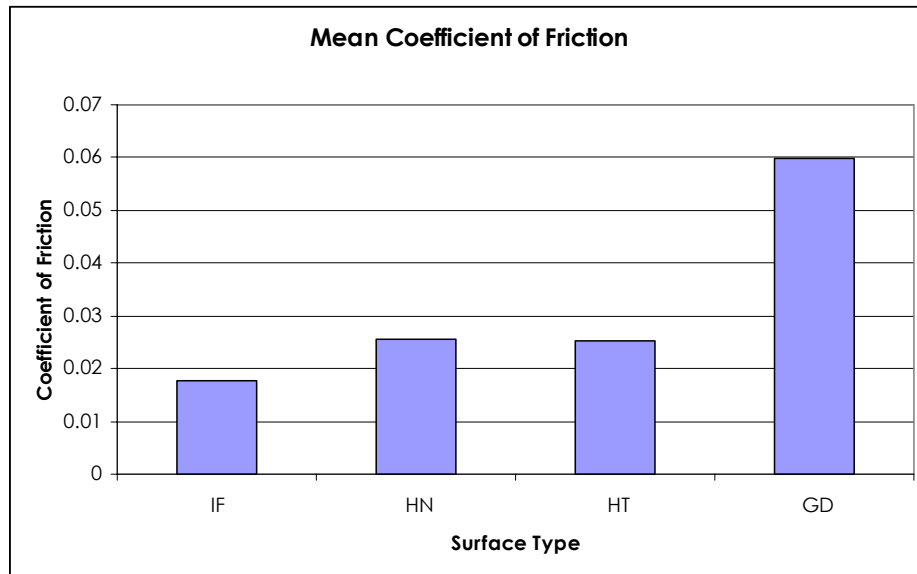


Figure 5.6: Mean Coefficients of Friction for Surfaces Studied

Possible correlation between the three-dimensional surface parameters and the mean coefficient of rolling/sliding friction for each surface was investigated. The amplitude parameter, S_q , which represents the root mean square deviation of asperities from the mean plane of a surface serves as a conservative estimate of the mean asperity height while the density of summits, S_{ds} , is assumed to represent the number of asperities per unit area. These two parameters seem to correlate most directly to the friction means seen in the rolling/sliding experiment. Table

5.6 shows the respective mean coefficient of rolling/sliding friction, S_q , and S_{ds} values for each surface. The S_q values of the GD and IF surfaces lie at the extremes of the surfaces measured as do their coefficients of rolling/sliding friction. However, if S_q was solely responsible for differences in the surfaces' frictional response, the HN surface would have a lower mean coefficient of friction than the HT surface. The data show that this is not the case and that roughness does not fully determine friction coefficient. Figure 5.7 shows the difference between a hypothetical roughness-only trend of coefficient of friction and the actual data acquired here. The S_{ds} parameter seems to also affect the frictional response and may account for its deviation from the expected trend of the surface roughness parameter, S_q . The other surface parameters calculated for each surface in Chapter 4 seem to correlate less directly to the friction data collected here. While they do help to identify certain aspects of the surfaces in question, they do not appear to directly affect the function of the surfaces within the scope of this work. The following section will offer possible explanation of these findings and identify possible sources of error encountered in this experiment.

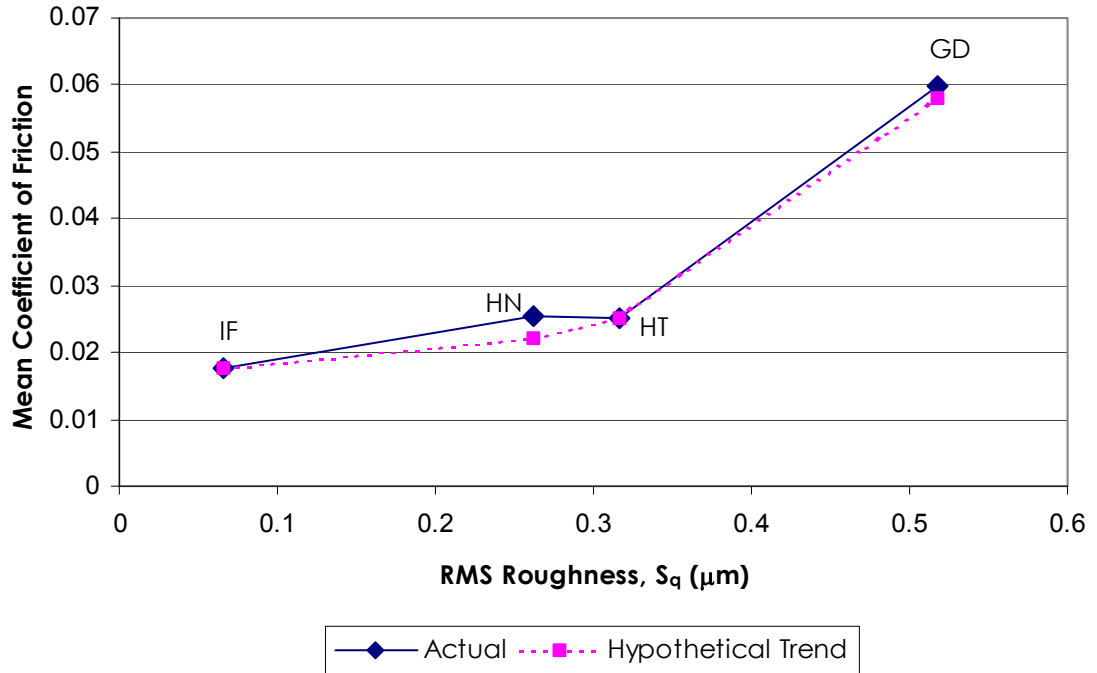


Figure 5.7: Hypothetical and Actual Friction Coefficients

Table 5.6: Coefficient of Friction and Relevant Surface Parameters

Surface	Mean coefficient of friction	$S_q(\mu\text{m})$	$S_{ds} (\text{mm}^{-2})$
GD	0.060	0.518	636.40
HN	0.025	0.262	2129.68
HT	0.025	0.316	92.25
IF	0.018	0.066	72.97

5.3 Evaluation of Results

Previously, in section 1 of this chapter, the lubricant film thickness of this experiment was found to be on the order of $1\mu\text{m}$. Owing to their respective surface roughness, the GD, HT, and HN surfaces were said to be in a mixed lubrication regime where the film thickness was of the same order as their asperity deviations from the mean plane [19]. This means

that in their line of contact, the tallest asperities are likely to contact one another, but that the fluid film is thick enough to prevent mechanical interference among the smaller peaks. Alternately, the IF surface acted in a full film EHL regime because its average peaks are an order of magnitude smaller than the film thickness [19].

This idea of full film separation for the IF surface coincides very well with the friction response seen in the experiment. First, the IF surface shows the lowest coefficient of rolling/sliding friction of any surface at all slide-to-roll ratios. Also, this coefficient changes very little as the surface speeds change for the IF surface. Because the overall speed of the two surfaces is reduced as the slide-to-roll ratio increases, the fluid is being forced into the converging gap less quickly and therefore builds up less pressure. This causes the lubricant film thickness to shrink. If any significant mechanical interference were present, the coefficient of friction would increase as the asperities came into deeper contact with one another. Since this is apparently not the case, only the shearing of the lubricant itself causes resistance to the surfaces' relative motion and it is, therefore, solely responsible for the friction seen from the IF surface. This provides a good minimum friction base to which the other surfaces can be compared. Since the other surfaces were tested under the same load and surface speed conditions as the IF surface, they will carry very similar

lubrication films. The shearing of this lubricant film results in a certain amount of friction, which the other surfaces are sure to exhibit similarly.

If every surface were to behave in a full film EHL manner, they would likely have very similar coefficients of friction due to the shear of their fluid films only. This is obviously not the case for this experiment. Therefore, other mechanisms must be present in the interaction of the other surfaces involved. Mechanical interference of surface asperities and surface adhesion play important roles in the friction response of contacting surfaces. The GD surface, with its relatively large S_q value, experiences significant mechanical interference even in the largest film thickness of the 0.1 slide-to-roll ratio tests. This is evident in its significantly higher friction coefficient as compared to the IF surface, which does not experience mechanical interference. Also, the high density of summits of the GD surface results in large surface area contact possibly causing significant adhesion in the surfaces. This adhesion contributes to the increased resistance to surface sliding and therefore increases the friction between the GD samples. In addition, as the slide-to-roll ratio increases and total surface speed drops, the fluid film thickness decreases introducing more asperities into mechanical contact and predictably raising the coefficient of rolling/sliding friction for the GD surface. This explains the steep slope of the GD surface plot in Figure 5.5. While the behavior of the GD surface illustrates the different mechanisms present in

the rolling/sliding contact of mixed lubrication, it does not help realize the significance of each. Is it the mechanical interference that most affects friction or is it adhesion? The friction response of the HN and HT surfaces will shed some light on the answer.

According to the same theories that govern the mechanical interference of the GD surface, the HT and HN surfaces should yield coefficients of friction between those of the IF and GD surfaces. The data clearly support this idea. The same theories would suggest that the HT surface should yield a higher coefficient of friction than its HN counterpart. However, the data clearly show very little difference between the responses of these surfaces and even suggest that the HT surface might exhibit a slightly smaller coefficient of friction. Inspection of the S_q and S_{ds} values for these surfaces shows that while the HT surface has about a 20% larger root mean square deviation from the mean plane, the density of summits of the HN surfaces is more than twenty times that of the HT surface. This would suggest that the adhesion of the drastically greater number of summits in the HN surface offsets its lower mechanical interference when compared with the HT surface. It would also seem that the S_{ds} parameter is much less sensitive than the S_q parameter in friction response because a very large increase in S_{ds} offsets a comparably small difference in S_q almost exactly.

As mentioned in Chapter 3 detailing the design and construction of the friction testing rig, the most significant sources of error in this experiment are the physical limitations of alignment and roundness in the apparatus and samples. Perfect horizontal and vertical alignment of the samples in their support bearings is simply not possible. Very thin shims were used to align the samples such that no light could be seen coming through the line of contact when the samples were just touching under no load, but tiny errors in alignment are surely present. Also, the sample support shafts were leveled relative to one another and along their lengths. More precise alignment equipment is available, however, its cost would exceed the resources for this project. The precision finished samples were made by The Timken Company, a commercial manufacturer of precision roller element bearings, and are considered to be at or near the maximum currently achievable commercially of precision in roundness and concentricity of the inner and outer diameters. Despite this fact, the samples are not perfectly produced and inherently still contain some errors in form. The filtration of the rotational frequency from the data was necessary to reduce the influence of these errors. Unfortunately, more subtle influences of some of the three-dimensional parameters discussed may be masked by these errors. In addition, the white light interferometry system used to characterize the different surfaces can only capture very small images of each surface at a time.

While it may be possible to combine many, many small pieces to construct a full surface map, the implementation of such large topographic surface matrices is impractical for both measurement and calculation purposes. Due to this fact, multiple small topographic maps were acquired for each surface and their parameter values averaged. While this would logically seem to represent the surface well, a more global surface characterization would certainly prove more accurate and possibly more valuable.

5.4 Summary

This chapter began with a description of the design parameters of the experimental work. The order and conditions of the tests were detailed and the coefficient of rolling/sliding friction calculations explained. Results of the experiment were then presented followed by explanation of those results. It was postulated here that the root mean square roughness parameter, S_q , very significantly affects the frictional response of a surface as does the density of summits, S_{ds} , albeit with less sensitivity. Also, it was suggested that an increase in slide-to-roll ratio reduces total surface speed and therefore lessens lubricant film thickness, also resulting in an increase in the coefficient of rolling/sliding friction for samples in the mixed lubrication regime. Finally, some sources of possible error in the data were identified and discussed.

Chapter 6

Conclusion

6.1 Summary of Findings

This experimental work revealed some very interesting results for the correlation of coefficient of rolling/sliding friction with slide-to-roll ratio and with some three-dimensional surface parameters for some precision machined surfaces currently in use in the roller bearing industries. The conclusions drawn are listed here:

- Differences between the coefficient of friction of the surfaces examined here are a result of differing levels of mechanical interference and surface adhesion.
- 2-D Roughness measurements alone are not sufficient to determine coefficient of friction; texture based 3-D parameters must also be considered.
- Coefficients of rolling/sliding friction are likely more sensitive to changes in RMS roughness (mechanical interference) than to changes in summit density (surface adhesion).

These conclusions broaden the scope of earlier works and show their applicability to these high precision surfaces (GD, HT, HN, IF) under rolling/sliding conditions. The remainder of this section is dedicated to brief discussion of these ideas.

Elastohydrodynamic lubrication film thickness calculations suggested that the lubricant films in this experiment were on the order of $1\mu\text{m}$. This film suggests that the lubrication regime for the IF surface was full film EHL in nature and that the other surfaces (GD, HT, HN) were under the influence of a mixed lubrication state because their differing RMS roughness values mean differing levels of mechanical interference are present. The coefficient of friction data for these surfaces supports this idea as the IF surface yields the lowest coefficient of friction at every slide-to-roll ratio. As slide-to-roll ratio was increased, the fluid films would shrink slightly and introduce more mechanical interference into the mixed lubrication systems. The increases in coefficient of friction with an increase in slide-to-roll ratio suggest that this is true.

It has been shown that the mechanisms responsible for the friction observed are mechanical interference of asperities, lubricant film shear, and surface adhesion. Because each surface was tested under the same load and speed conditions, they share very similar fluid film effects [19]. The changes in the friction coefficients observed in the different surfaces, then, were attributed to their different mechanical interference patterns and levels of surface adhesion.

The root mean square deviation of asperities from the mean plane factor, S_q , was used to identify mechanical interference between peaks in the topography of the surfaces. The greater the S_q value of the surface,

the more asperities would become involved in mechanical interference and the deeper that interference would become, thus increasing the coefficient of rolling/sliding friction. This result parallels Koura's [27] findings, but for 3-D parameters and rolling/sliding contact. In addition, the density of summits factor, S_{ds} , governed the amount of surface area that was involved in the contact and therefore determined the adhesion between the test surfaces. As the density of summits increased, the number of asperities in close proximity to each other increased causing more adhesion between the surfaces and subsequently increasing the observed coefficient of rolling/sliding friction. This dependence of friction on three-dimensional summit density coincides with Cann et al's [28] work with two-dimensional parameters.

The sensitivity of these factors was also explored and it was postulated that small changes in mechanical interference might be roughly equivalent to very large changes in adhesion. This suggests that the coefficient of friction of the surfaces tested here are much more sensitive to changes in the S_q parameter than they are to changes in the S_{ds} parameter. This effect provides insight into the contact between surfaces and could help further optimize the coefficient of friction of surfaces.

6.2 Future Work

To further build upon the information presented in this thesis, some possible topics of future work are presented. First, using the existing apparatus and data acquisition systems more resources could be allocated to the exploration of avenues to reduce some of the errors mentioned in Chapter 5. With improvements to the alignment systems, perhaps more subtle effects of different three-dimensional surface parameters would become apparent. Also, the construction of a more robust friction testing rig could yield further study of the similar factors studied here under more strenuous loads. Reduced lubricant film thicknesses would result and therefore more plastic deformation would occur in mixed lubrication regimes. This would also make possible a study of wear and its effect not only on the coefficient of rolling/sliding friction of the precision finished surfaces, but also on the changes in three-dimensional surface parameters that results from significant plastic deformation. Since highly specialized computer models currently exist that accurately represent the friction of precision finished surfaces [33], further testing of the influence of three-dimensional surface parameters on friction may be conducted through simulations. From these other avenues of study, ideal combinations of each parameter could be devised for a desired friction response. Finally, processes to produce such idealized surfaces could be reverse engineered for manufacturing

facilities that would approach ideal surface characteristics for desired functionality. Certainly, gains against friction that could result from future work would be worth the resources spent to attain them.

Appendix A

Matlab Code for Friction Data Analysis

```
%Load Raw Data as 'data'
L_t=data(:,3);
T_tb=data(:,4);
T_t=T_tb - .23396;

[Y] = butter_filter(L_t)
Yl=Y %+ mean(L_t);
% Plot
L_f=Yl(500:10000);
figure(1)
plot(L_t(500:10000), 'r.')
hold on;

plot(L_f,'b.'), grid on;
title(' Filtered load data');

[Y] = butter_filter(T_t)
Yl=Y %+ mean(T_t);
T_f=Yl(500:10000);
figure(2)
plot(T_t(500:10000), 'r.')
hold on;

plot(T_f,'b.'), grid on;
title('Filtered Torque data');

F_f=T_f./0.0382
N_f=L_f.*0.453*9.81
mu_f=F_f./N_f

L_t=L_t(500:10000)
T_t=T_t(500:10000)

F_t=T_t./0.0382
N_t=L_t.*0.453*9.81
mu_t=F_t./N_t

figure(3)
plot(mu_t, 'r.')
hold on;
plot(mu_f,'b.')

title('Coefficient of friction data');
unfiltered_mean_mu=mean(mu_t)
unfiltered_stddev_mu=std(mu_t)
filtered_mean_mu=mean(mu_f)
filtered_stddev_mu=std(mu_f)
```

ButterFilter Subroutine

```
function [Y] = butter_filter(x)

if (nargin == 1)
else
    error('Must provide only 1 argument')
end

Fs = 1000;                %Sampling Frequency.
fc=15                    %low-pass cutoff set to 15 Hz.
Wn = 1/[0.5*Fs/fc]

N = 8;                  %N identifies the order of filter.
[B,A] = butter(N,Wn,'low'); %Create an Nth order
Butterworth filter.
Y = filtfilt(B,A,x);    %Forward/reverse filtering of
input data (x).
```

Surface Characterization Code

Initial Matrix Creation

```
% load the file
clear all
load GD75a1L.zyg
inp=GD75a1L;
[size,col]=size(inp);
m= 320
n=240
j=1
k=1
%Initialize result
res=zeros(m,n);
x=inp(:,1);
y=inp(:,2);
z=inp(:,3);
for i=1:size-1

    if (x(i+1)== x(i))
        res(k,j)= z(i);
        k=k+1;

    else
        j=j+1;
        k=1;
    end
end
end
```

```
plot3(x,y,z)
```

Extraction of Valid Data

```
z=zeros(250,200);
for i=1:250
    for j=1:200
        z(i,j)=res(i,j);
    end
end
```

Fitting to Flat Plane

```
[m,n]=size(z)
deltax=2.2*10^-6

deltay=deltax
p=1
u=zeros(m*n,1)
v=zeros(m*n,1)
q=zeros(m*n,1)
V=zeros(m*n,1)
for i=1:m
    for j=1:n
        u(p)=(i-1)*deltax;
        v(p)=(j-1)*deltay;
        q(p)=z(i,j);
        p=p+1;
    end
end
for i=1:m*n
    V(i,1)=1;
    V(i,2)=u(i);
    V(i,3)=v(i);
    V(i,4)=u(i)^2;
    V(i,5)=u(i)*v(i);
    V(i,6)=v(i)^2;
end
V1=V'*V;
V2=V1^-1;
B=V2*V';
A=B*q;
for i=1:m
    for j=1:n

Z(i,j)=z(i,j)-(A(1) +A(2)*(i-1)*deltax + A(3)*(j-1)*deltax +
A(4)*(((i-1)*deltax)^2 )+ A(5)*((i-1)*deltax)*((j-1)*deltay)
+ A(6)*((j-1)*deltay)^2);
```

```

end
end
mesh(Z)

```

Calculation of S_q , S_{sk} , and S_{dq}

```

[m,n]=size(Z)
z=Z;
sum=0
sum1=0
for j=1:n
    for i=1:m
        sum = sum + z(i,j)^2;
    end
end

sq=(sum/(m*n))^0.5
% calculate ssk
for j=1:n
    for i=1:m
        sum1 = sum1 + z(i,j)^3;
    end
end
Ssk=sum1/(m*n*(sq^3))
deltax=2.2*10^-6;
deltay=2.2*10^-6;
sum=0;
for j=2:n
    for i=2:m
        sum = sum + ((z(i,j)-z(i-1,j))/deltax)^2 + ((z(i,j)-
z(i,j-1))/deltay)^2;
    end
end
sdq=(sum/((m-1)*(n-1)))^0.5

```

Calculation of S_t and S_{a1}

```

AACF1=xcorr2(Z);
AACF=zeros(249,199);
for i=126:374
    for j=101:299
        AACF(i-125,j-100)= AACF1(i,j);
    end
end
AACF(125,100)

z=AACF/max(max(AACF));
[m,n]=size(AACF)
%y=zeros(3,200);
o=1;
for i=1:m

```

```

        for j=1:n
            if z(i,j)<0.205& z(i,j)>0.195
                disp(z(i,j));
                y(3,o)= z(i,j);
                y(1,o)= i;
                y(2,o)=j;
                o=o+1;
            end
        end
    end
end

[m,n]=size(y)
out=zeros(n,2);
deltax=zeros(n,1);
deltay=zeros(n,1);
out=zeros(n,2);
% calculate the distance
for i=1:n
    for j=1:m
        deltax(i)=abs(y(1,i)-125)*(2.2*10^-6);
        deltay(i)=abs(y(2,i)-100)*(2.2*10^-6);
        out(i,1)=y(3,i);
        out(i,2)=(((deltax(i)^2+deltay(i)^2))^0.5)/10^-6;
    end
end
st=min(out(:,2))/max(out(:,2))
sal=min(out(:,2))

```

Calculation of S_{ds}

```

o=1
% give the value of k (no. of units of deltax+1)
[m,n]=size(Z)
k=25
eta=zeros(k,k)

for p=1:m-k+1;
    for q=1:n-k+1;
        for i=p:p+(k-1)
            for j=q:q+(k-1)
                eta(i-p+1,j-q+1)=Z(i,j);
            end
        end
        if eta((k+1)/2,(k+1)/2)==max(max(eta))
            o=o+1;
        end
    end
end
end
deltax=2.2*10^-6
sd=(o*10^-6)/((m-1)*deltax*(n-1)*deltax)

```

Appendix B

Experimental Design

HT 75A	HT 75B	GD 75A	GD 75B	HN 75A	HN 75B	IF 75A	IF 75B	
	3	3	3	2	2	1	1	3
	1	1	1	3	3	4	4	4
	4	2	2	4	4	2	3	1
	2	4	4	1	1	3	2	2
	1	4	3	4	3	1	2	3
	2	3	2	2	2	4	3	1
	4	2	1	1	4	3	4	4
	3	1	4	3	1	2	1	2
	3	1	1	1	4	4	1	1 S/R Ratios
	2	4	2	4	2	3	4	4
	1	2	4	2	1	1	3	3
	4	3	3	3	3	2	2	2
	2	2	1	4	4	4	2	1
	4	4	3	2	3	3	3	4
	3	3	2	1	2	1	1	2
	1	1	4	3	1	2	4	3
	3	3	3	2	2	1	1	3
	1	1	1	3	3	4	4	4
	4	2	2	4	4	2	3	1
	2	4	4	1	1	3	2	2

Order of surface testing

1=HT 2=GD 3=HN 4=IF
 4 3 2 1 4 1 3 2

Full Data Set from Friction Testing

75lb load IF	HN	HT	GD
S/R ratio	Mean μ of 10 sec. Run		
0.1	0.0246	0.0274	0.0222
0.1	0.0209	0.0275	0.0182
0.1	0.0226	0.0273	0.0234
0.1	0.0176	0.0275	0.0159
0.1	0.0193	0.0261	0.0154
0.2	0.0247	0.03	0.0208
0.2	0.024	0.0327	0.0196
0.2	0.0213	0.0295	0.0186
0.2	0.0214	0.0316	0.0195
0.2	0.0193	0.03	0.0179
0.3	0.0251	0.0308	0.0231
0.3	0.0269	0.0346	0.0203
0.3	0.0231	0.0316	0.0201
0.3	0.0225	0.0343	0.0201
0.3	0.0214	0.0311	0.0195
0.4	0.0259	0.0308	0.0224
0.4	0.0263	0.0316	0.0213
0.4	0.025	0.0316	0.0242
0.4	0.0261	0.0365	0.0216
0.4	0.023	0.032	0.022
0.1	0.015	0.0241	0.0249
0.1	0.0131	0.0185	0.0239
0.1	0.009	0.0173	0.0238
0.1	0.0104	0.0162	0.0269
0.1	0.0081	0.0166	0.0269
0.2	0.0137	0.0224	0.0267
0.2	0.0113	0.019	0.0267
0.2	0.0131	0.0185	0.0307
0.2	0.0096	0.0193	0.0299
0.2	0.008	0.0181	0.032
0.3	0.0203	0.0216	0.0306
0.3	0.0131	0.0221	0.0284
0.3	0.0152	0.0204	0.0325
0.3	0.0095	0.0208	0.0336
0.3	0.0084	0.0205	0.0361
0.4	0.017	0.0221	0.0296
0.4	0.0145	0.0214	0.0298
0.4	0.0115	0.0213	0.0321
0.4	0.0117	0.0226	0.0362
0.4	0.0101	0.0198	0.0415

References

- [1] ASME B46.1, Surface Texture, 1985.
- [2] ANSI, Surface Texture: Surface Roughness, Waviness and Lay, American Standard ANSI 8.46.1, 1985
- [3] ISO, Surface Roughness - Terminology - Part 1: Surface Parameters, International Standard ISO 4287/1, 1984.
- [4] Thomas, T.R. Rough Surfaces, Longman, Inc., USA, 1982.
- [5] W.P. Dong, P.J. Sullivan and K.J. Stout, "Comprehensive study of parameters for characterizing three-dimensional surface topography - III: Parameters for characterizing amplitude and some functional properties," *Wear*, 178, 1994, 29-43.
- [6] W.P. Dong, E. Mainsah, K.J. Stout and P.J. Sullivan, "Three-dimensional surface topography - Review of present and future trends," in K.J. Stout (ed.), Three-dimensional Surface Topography: Measurement, Interpretation and Applications, A Survey and Bibliography, Penton, 1994, pp. 65-85.
- [7] W.P. Dong, P.J. Sullivan and K.J. Stout, "Comprehensive study of parameters for characterizing three-dimensional surface topography - IV: Parameters for characterizing spatial and hybrid properties," *Wear*, 178, 1994, 45-60.

- [8] W.P. Dong and K.J. Stout, "Two-dimensional fast Fourier transform and power spectrum for surface roughness in three dimensions," *Proc. I. Mech. E.*, Vol. 209, pp. 381-391, 1995.
- [9] T. Y. Lin, L. Blunt and K. J. Stout, "Determination of proper frequency bandwidth for 3D topography measurement using spectral analysis. Part I: isotropic surfaces," *Wear*, 166, 1993, 221-232.
- [10] J. Peklenik, "Investigation of Surface Typology, *Ann. CIRP* Vol. 15, pp. 381-385, 1967.
- [11] J. Peklenik, "New Developments in Surface Characterization and Measurements by Means of Random Analysis, *Proc. I. Mech. E.* Vol. 182, Part 3K, pp. 108-126, 1967/68.
- [12] D.J. Whitehouse and J.F. Archard, "The Properties of Random Surfaces of Significance in Their Contact," *Proc. R. Soc. London, Ser. A*, 316, 1970, 97-121.
- [13] P.R. Nayak, "Random Process Model of Rough Surfaces," *J. Lubr. Technol. Trans. ASME*, July 1971, pp. 398-407.
- [14] P.R. Nayak, "Some Aspects of Surface Roughness Measurement," *Wear*, Vol.26, 1973, 165-174.
- [15] I. Sherrington and G. W. Howarth, "Approximate Numerical Models of 3-D Surface Topography Generated Using Sparse Frequency Domain Descriptions," *Int. J. Mach. Tools Manufact.* Vol. 38, Nos.5-6, pp. 599-606, 1998.

- [16] I. Sherrington and E.H. Smith, "Surface Topography, Area1 Fourier Analysis of Surface Topography. Part 1: Computational Methods and Sampling Considerations," *Surf. Topography*, 3 (1), 1990, 43-68.
- [17] Patir, N., and Cheng, H. S., "An Average Flow Model of Determining Effects of Three-Dimensional Roughness on Partial Hydrodynamic Lubrication," *Trans. ASME Jour. of Lubrication Technology*, 1978, Vol. 100, 12-16.
- [18] M. Esfahanian and B. J. Hamrock, "Fluid-Film Lubrication Regimes Revisited," *Tribology Transactions*, 1991, Vol. 34, 628-632.
- [19] Dong Zhu, "Effect of Surface Roughness on Mixed EHD Lubrication Characteristics," *Tribology Transactions*, 2003, Vol. 46, 44-48.
- [20] B. J. Hamrock and H. S. Cheng, "Characterization of Elastohydrodynamic Lubrication," *Achievements in Tribology*, 1990, 57-73.
- [21] Dong Zhu and H. S. Cheng, "Effect of Surface Roughness on Pressure Spike and Film Constriction in Elastohydrodynamically Lubricated Line Contacts," *Tribology Transactions*, 1990, Vol. 33, 267-273.
- [22] J. A. Greenwood and J. B. Williamson, "Contact of Nominally Flat Surfaces," *Proc. Roy. Soc. Lond.*, 1966, A295, 300-319
- [23] Hisakado, T., Influence of Surface Roughness on Friction and Wear in Boundary Lubrication," *J. Mech. Eng. Sci.*, 1978, Vol. 20, 247-254.

- [24] Johnson, K. L., Greenwood, J. A., and Poon, S. Y., "A Simple Theory of Apserity Contact in EHL," *Wear*, 1972, Vol. 19, 91-108.
- [25] E. Rabinowicz, Friction and Wear of Materials, 2nd Edition, John Wiley & Sons, 1995.
- [26] Yeau-ren Jeng, "Experimental Study of the Effects of Surface Roughness on Friction," *Tribology Transactions*, Volume 33. 1990, 3,402-409.
- [27] Koura, M. M., "The Effect of Surface Texture on Friction Mechanisms," *Wear*, 1980, Vol. 63, 1-12.
- [28] Cann, P., Ioannides, E., Jacobson, E., and Lubrecht, A. A., "Lambda Ratio- A Critical Re-examination," *Wear*, 1994, Vol. 175, 177-188.
- [29] K. Holmberg, "Influence of Surface Topography on Friction in Lubricated Contacts," *Proc. of 11th Leeds-Lyon Symposium on Tribology*, pp 45-49, 1984.
- [30] H. S. Cheng, "The Lubrication of Rough Surfaces," *Proc. of 11th Leeds-Lyon Symposium on Tribology*, pp 11-20, 1984.
- [31] J. H. Tripp and B. J. Hamrock, "Surface Roughness Effects in Elastohydrodynamic Contacts," *Proc. of 11th Leeds-Lyon Symposium on Tribology*, pp 11-20, 1984.
- [32] X. Ai and H. S. Cheng, "The Effects of Surface Texture in Point Contacts," *Journal of Tribology*, Jan. 1996, Vol. 118, 59-66.

- [33] D. Zhu and Y. Hu, "A Computer Program for Prediction of EHL and Mixed Lubrication Characteristics, Friction, Subsurface Stresses and Flash Temperatures Based on Measured 3-D Roughness," *Tribology Transactions*, Vol. 44, 3, 383-390, 2001.
- [34] Y. Z. Hu and D. Zhu, "A Full Numerical Solution to the Mixed Lubrication in Point Contacts," *Tribology Transactions*, Jan. 2000, Vol. 122, 1-9
- [35] A. Lubrecht, W. E. ten Napel and R. Bosma, "The Influence of Longitudinal and Transverse Roughness on Elastohydrodynamic Lubrication of Circular Contacts, *Journal of Tribology*, Jan. 1988, Vol. 110, 421-426.
- [36] R. Singh and S. N. Melkote, "Frictional Response of Precision Finished Surfaces under Sliding Conditions," submitted *Wear*.
- [37] W.P. Dong, E. Mainsah, and K.J. Stout, "Reference Planes for the Assessment of Surface Roughness in Three Dimensions," *Int. J. Mach. Tools Manufact.* Vol. 35, No.2, pp. 263-271, 1995.
- [38] R. S. Zhou and F. Hashimoto, "A New Rolling Contact Surface and 'No Run-in' Performance Bearings," *Transactions of the ASME*, Vol. 117, 166-170, 1995.
- [39] D. Dowson and A. Toyoda, "A Central Film Thickness Formula for EHD Line Contacts," *Leeds-Lyon Symposium on Tribology*, pp. 60-65, 1978.

- [40] S. Bair and F. Qureshi, "Accurate Measurements of Pressure-Viscosity Behavior in Lubricants", *STLE Tribology Transactions*, Vol. 45, 2002, pp. 390-396.
- [41] S. Bair, "A More Complete Description of the Shear Rheology of High-Temperature, High-Shear Journal Bearing Lubrication," submitted to *STLE Tribology Transactions*.
- [42] D. Dowson, "The inlet boundary condition," *Leeds-Lyon Symposium on Tribology*, pp. 143-152, 1975.
- [43] B. B. Mikic, "Thermal Contact Conductance: Theoretical Considerations," *Int. J of Heat and Mass transfer*, 17, 205, 416-417